UNIVERSITÀ DEGLI STUDI DI PADOVA

Dipartimento di Fisica e Astronomia "Galileo Galilei"

Master Degree in Astrophysics and Cosmology

Final Dissertation

Impact of core-collapse supernova models on the population of binary black holes

Thesis Supervisor	Candidate
Prof. Michela Mapelli	Francesco Iraci
Thesis Co-Supervisor	
Dott. Giuliano Iorio	

Academic Year 2021/2022

Abstract

Uncertainties about the description of core-collapse supernova mechanisms still make our understanding of the mass spectrum of black holes difficult. Thanks to the numerous detections of gravitational wave events, the mass distribution of black holes finally represent an observable and can be used to test stellar evolution. In my thesis I have considered different core-collapse supernova models and I have studied their effect on the population of binary black hole systems with the population synthesis code SEVN [Spera et al., 2019]. I have simulated the evolution of a set of single and binary stars with fixed metallicity in the range $[10^{-4}, 2 \cdot 10^{-2}]$, no spin, pair-instability model taken from Mapelli et al. [2020] and Farmer et al. [2019], and three different core-collapse supernova models: rapid, delayed and compactness with different compactness thresholds ξ_t.

The single stellar evolution scenario is useful to understand the role of metallicity, pair-instability supernova and dredge-up events on the black holes population. The binary case, instead, shows the effect of mass transfer episodes on the spectrum.

The impact of core-collapse supernova choice is mainly seen in the production of black holes in the lower edge of the mass distribution. With the rapid model the minimum black hole mass is $5\,M_\odot$, which reproduces the observed mass gap between neutron stars and black holes; delayed model does not predict any gap, having the transition at $3\,M_\odot$; with compactness model instead the minimum mass is determined by the threshold of compactness chosen. It goes from $\approx 3\,M_\odot$ for $\xi_t = 0.1$ to $\approx 25\,M_\odot$ for $\xi_t = 0.5$. Each black hole mass spectrum shows a peak around $10\,M_\odot$ (except for $\xi_t = 0.5$) which can also be found in the rate of mergers obtained from the LIGO/Virgo data [Abbott et al., 2022].

Finally I have discussed the incidence of each supernova type for each core-collapse supernova model. I have found that the relative rate between electron-capture supernovae and core-collapse supernovae is in the range 2% - 4%, which is in good agreement with observational results of Thompson et al. [2009].

Contents

1 Introduction **1**

2 Binary black holes from gravitational waves **3**
2.1 LIGO and VIRGO . . . 3
2.2 Inspiral of compact binaries . . . 3
2.3 Mass distribution of binary black holes . . . 5

3 Formation of black holes and binary black holes **7**
3.1 Stellar evolution for massive stars . . . 7
3.2 Binary stellar evolution . . . 8
3.3 Supernova classification . . . 11
3.3.1 Core collapse supernovae observations . . . 11
3.3.2 Theory of core-collapse supernova . . . 12
3.3.3 Electron-capture supernova (ECSN) observations . . . 13
3.3.4 Electron-capture supernova theory . . . 14
3.3.5 Pair instability and pulsational pair instability supernovae . . . 14

4 Methods **17**
4.1 SEVN . . . 17
4.1.1 Stellar tracks . . . 18
4.1.2 Core collapse supernova models . . . 18
4.1.3 Pair instability and pulsational pair instability . . . 19
4.1.4 Initial conditions . . . 20

5 Results **23**
5.1 Single star evolution (SSE) . . . 23
5.1.1 Discussion . . . 24
5.2 Binary star evolution (BSE) . . . 30
5.2.1 Rapid and Delayed . . . 32
5.2.2 Compactness . . . 32
5.2.3 Supernova channels . . . 36
5.2.4 Discussion . . . 36

6 Conclusions **43**

Chapter 1

Introduction

Gravitational wave (GW) events detected with ground based interferometers LIGO, Virgo, and KAGRA (LVK) provide crucial insights on the astrophysics of binary black holes (BBHs) systems. After the second-half of LVK third observing run (O3b) that took place between November 2019 and March 2020, the total number of observed events reached 90 since LIGO–Virgo operations began. Important source properties can be studied by analysing gravitational wave signals and in particular it is possible to determine the masses of the compact objects in the binary system. This allows to build the mass distribution of binary black holes (BBHs) with an accuracy increasing with the number of detections. Since the number of events is becoming statistically relevant, the black hole (BH) mass spectrum can be used to test stellar evolution models.

In my thesis, I have studied the BH mass spectrum obtained using the population synthesis code SEVN (Spera et al. [2019]). In particular I run a set of simulations changing the metallicity of the initial population of stars, the core-collapse supernova (CCSN) mechanism and the pair instability model. Metallicity varies from 2×10^{-2} to 10^{-4} in order to have a complete landscape of remnants coming from metal rich and metal poor stars. Different CCSN models are implemented in the code SEVN and I chose to study three of them: rapid, delayed [Fryer et al., 2012] and compactness [O'Connor and Ott, 2011]. For the description of pair and pulsational pair instability I adopted the two main models implemented in SEVN: M20 from Mapelli et al. [2020] and F19 from Farmer et al. [2019]. The comparison of the mass spectrum of these models is concentrated on the amount of BHs produced at low masses ($2 - 5\,\mathrm{M}_\odot$), because of the dearth of compact objects observed in that range, and on the upper mass gap ($50 - 150\,\mathrm{M}_\odot$) predicted by the theory of pair instability (PI). Because of the crucial impact of CCSN models on the population of BHs, it is important to understand which one better represent the data to interpret future gravitational wave signals coming from BBH coalescence.

Chapter 2

Binary black holes from gravitational waves

2.1 LIGO and VIRGO

In 1916, the year after the final formulation of general relativity, Albert Einstein predicted the existence of grvitational waves. He found that the linearized weak-field approximation had wave solution and it was generated by the time variation of the mass quadrupole moment of the source. A century later, Einstein's prediction has been verified with the first direct gravitational wave event ever detected. On September 14th, 2015 the two detectors of the Laser Interferometer Gravitational Wave Observatory (LIGO) simultaneously observed a gravitational wave signal coming from the coalescence of a BBH system [Abbott., 2016]. Laser interferometers measure gravitational wave strain as a difference in length of its orthogonal arm which are of the same length $L_x = L_y = L$. A passing GW alters the arm length such that the measured difference is proportional to the GW strain amplitude $h(t)$: $\Delta L = \delta L_x - \delta L_y = h(t)L$. This length variation alters the phase difference of the two light fields that are propagating along the x and y arms. Then they recombine at the beam splitter, transmitting an optical signal proportional to $h(t)$ to the output photodetector. A schematic representation of the detector setup is shown in Figure 2.1

2.2 Inspiral of compact binaries

The typical example of a system which emits GWs is a binary made of two compact objects (usually neutron star (NS)- NS or BH-BH). For these systems it is convenient to define the chirp mass:

$$M_c = \frac{(m_1 m_2)^{\frac{3}{5}}}{(m_1 + m_2)^{\frac{1}{5}}} \tag{2.1}$$

where m_1 and m_2 are the masses of the binary components. Considering the approximation of circular orbit, it is possible to have a picture of the consequences of GW emission. Let us start by noticing that the system described is stable and bound by the gravitational potential. In this case it is possible to use the virial theorem which allows us to write the

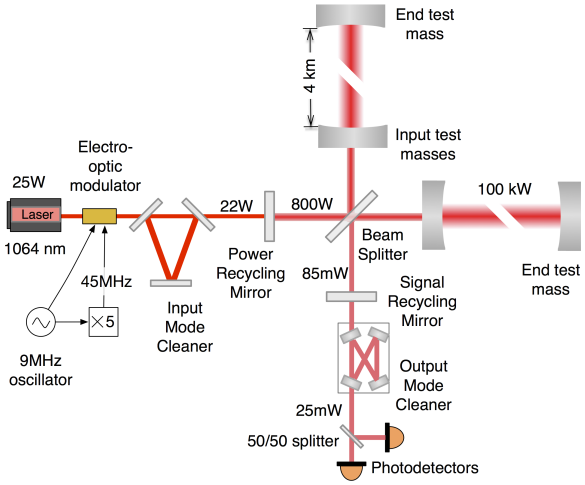

Figure 2.1: Advanced LIGO layout. Image of Sengupta [2016]

total energy as:

$$E_{tot} = E_k + E_p = \frac{E_p}{2} \tag{2.2}$$

$$= -G\frac{m_1 m_2}{2R} \tag{2.3}$$

where R is the radius and G the universal gravitational constant. Taking the time derivative:

$$\frac{dE}{dt} = \frac{Gm_1m_2}{2R^2}\frac{dR}{dt} \Rightarrow \dot{R} = \frac{2R^2}{Gm_1m_2}\dot{E} = -\frac{2R^2}{Gm_1m_2}\dot{E}_{gw} \tag{2.4}$$

Thus the energy of the system is decreased by gravitational wave emission and at the same time the radius shrinks, the orbital frequency increases and so does the emission of gravitational waves. It is a runaway process which, on a sufficiently long time-scale, leads to the coalescence of the binary system. This assumption is legitimate as long as $\dot{\omega}_s \ll \omega_s^2$ and it is called *quasi-circular orbit motion* [Maggiore, 2007]. The GW frequency can be found to be related to the chirp mass:

$$\dot{\omega}_{gw} = \frac{12}{5}2^{1/3}\left(\frac{M_c G}{c^3}\right)^{5/3}\omega_{gw}^{11/3} \tag{2.5}$$

with $\omega_{gw} = 2\pi f_{gw}$ and f_{gw} being the gravitational wave frequency. By integrating and then inverting (2.5) it is possible to find the time to coalescence $-\tau = t - t_{coal}$, with t_{coal} time at which the frequency diverges:

$$\tau = \frac{5}{256}\left(\frac{1}{\pi f_{gw}}\right)^{8/3}\left(\frac{c^3}{GM_c}\right)^{5/3} \tag{2.6}$$

and then the relation between radius R and τ can be found to be:

$$R(\tau) = R_0\left(\frac{\tau}{\tau_0}\right)^{1/4} \tag{2.7}$$

where R_0 is the value od R at initial time τ_0. In the end, the gravitational wave strain can be written as:

$$h_+(t) = \frac{1}{r}\left(\frac{GM_c}{c^2}\right)^{5/4}\left(\frac{5}{c\tau}\right)^{1/4}\frac{1+\cos^2\theta}{2}\cos\phi(\tau) \tag{2.8}$$

$$h_x(t) = \frac{1}{r}\left(\frac{GM_c}{c^2}\right)^{5/4}\left(\frac{5}{c\tau}\right)^{1/4}\cos\theta\sin\phi(\tau) \tag{2.9}$$

where h_+ and h_x are the two polarizations, θ is the azimutal angle between the observer and the center of orbital plane and $\phi(\tau) = \int_{t_0}^{t} dt' \omega_{\rm gw}(t')$.

The chirping signal described by $h(t)$ has been found for the first time in September 2015 as shown in figure 2.2 and from that moment on, 90 gravitational wave events have been measured. Sources of these signal represent the most exotic objects in the universe. The study of their properties and formation channels is one of the most challenging aspect in modern astrophysics.

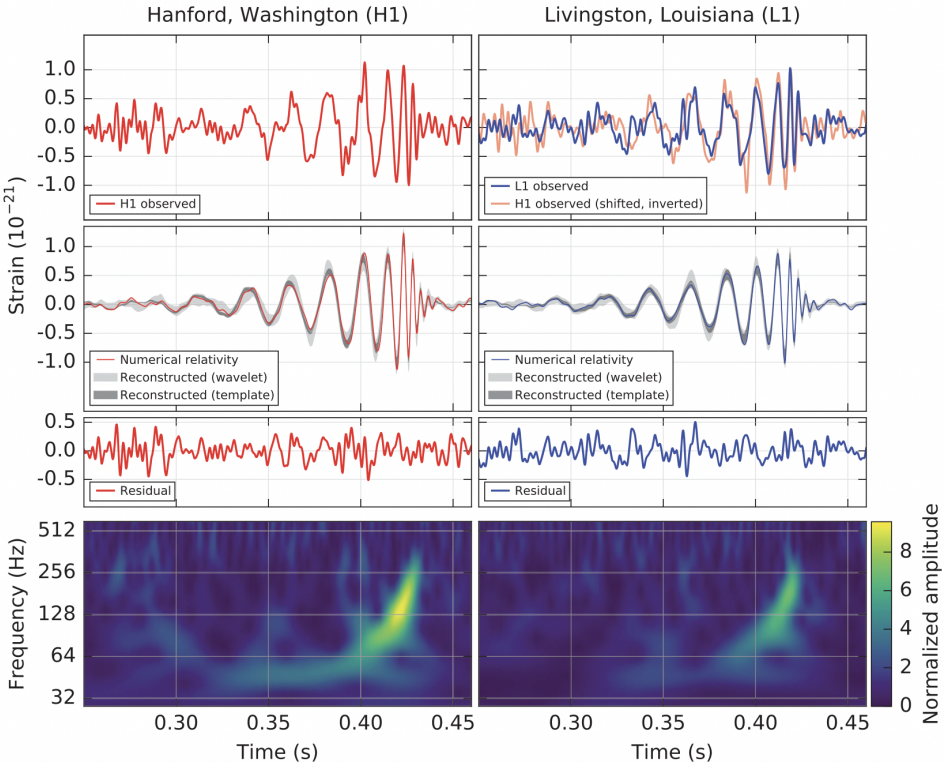

Figure 2.2: First ever gravitational wave event GW150914 detected by LIGO Hanford H1 and Livingston L1. Image of Abbott. [2016]

2.3 Mass distribution of binary black holes

After the third campaign of observations, the number of gravitational wave events raised to 76 in O3a, then to 90 in O3b. With this amount of information, LVK collaboration was able to produce a confident description of the mass distribution of binary black holes [Abbott et al., 2022]. In figure 2.3 they show the merger rate $d\mathcal{R}/dm_1$ (the number

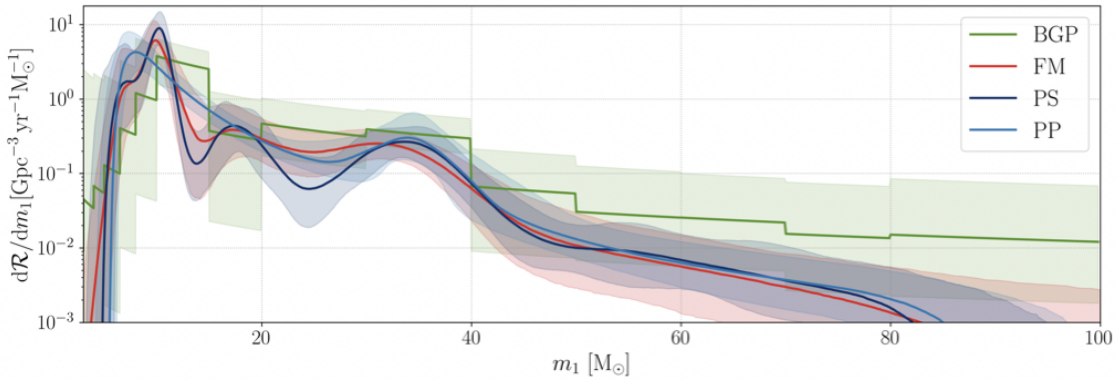

Figure 2.3: Rate of mergers per Gpc^3, per year and per unit mass as a function of the primary mass. Different lines represent different non-parametric model. Image of Abbott et al. [2022]

of merger events per Gpc^3, per year and per unit mass), as a function of the primary mass m_1. The distribution present multiple peaks, with the one at $\sim 10\,M_\odot$ and the other at $\sim 35\,M_\odot$ in common to all models. The substructures present in the merger rate were also found by Tiwari and Fairhurst [2021] after the analysis of gravitational waves transient catalog 2 (GWTC-2). The best way to describe the mass distribution is by using an unbroken power law with a global maximum at $10\,M_\odot$. If these structures will be confirmed by future GW observations, they will provide a deeper insights on the formation channels of binary black holes.

In next chapter I will present the evolution of massive stars both in isolated and binary systems. The final fate of these stars is typically to form a BH or a NS.

Chapter 3

Formation of black holes and binary black holes

3.1 Stellar evolution for massive stars

Stars with zero-age main sequence (ZAMS) mass in the range $10-100\,M_\odot$ are the so called *massive stars*. On the main sequence, such massive stars have non-convective surfaces, convective cores and are powered by the CNO cycle [Adelberger et al., 2011]. In this process, reactions are characterized by large Coulomb barriers and the energy production has a steeper dependence on temperature ($\epsilon \propto T^{18}$) with respect to the the pp-chain ($\epsilon \propto T^4$), the other possible hydrogen burning process which happens for low-mass stars.

The evolution of massive stars is marked by a sequence of hydrostatic burning stages in the interior, where hydrostatic means that there is balance between the gravitational force, directed inward, and the pressure gradient, which pushes outward. The simple equation that describe this process is:

$$\underbrace{-G\frac{M_r\,\rho}{r^2}}_{\text{Gravitational force per unit volume}} = \underbrace{\frac{dP}{dr}}_{\text{Pressure gradient}} \tag{3.1}$$

where M_r is the gravitational mass at radius r, ρ is the density, P is the pressure.

When all the fuel is extinguished, the core contracts and heats up because no force is opposing the gravitational collapse. When the temperature becomes high enough, then the second nuclear burning phase begins, bringing the system back to the hydrostatic equilibrium. This is the so called *mirror principle* [Hekker et al., 2020]. In fact, after the first nuclear burning stage, the core is mostly occupied by helium, while hydrogen will be present in a burning shell above the core. The mirror principle occurs whenever a star has an active shell burning source. The shell itself acts as a mirror between the core and the envelope to maintain thermal equilibrium: the expansion of the envelope corresponds to a compression of the core and vice versa.

The sequence of nuclear burning phases is showed in Table 1 of Woosley et al. [2002]. Evolution beyond helium burning is greatly accelerated by thermal neutrino losses, especially from electron-positron pair annihilation. It is the temperature sensitivity of these neutrino losses, combined with the need to go to higher temperatures in order to burn fuels with larger charge barriers, that leads to a rapid acceleration of the stellar evolution during carbon, neon, oxygen, and silicon burning, the latter typically taking only a day

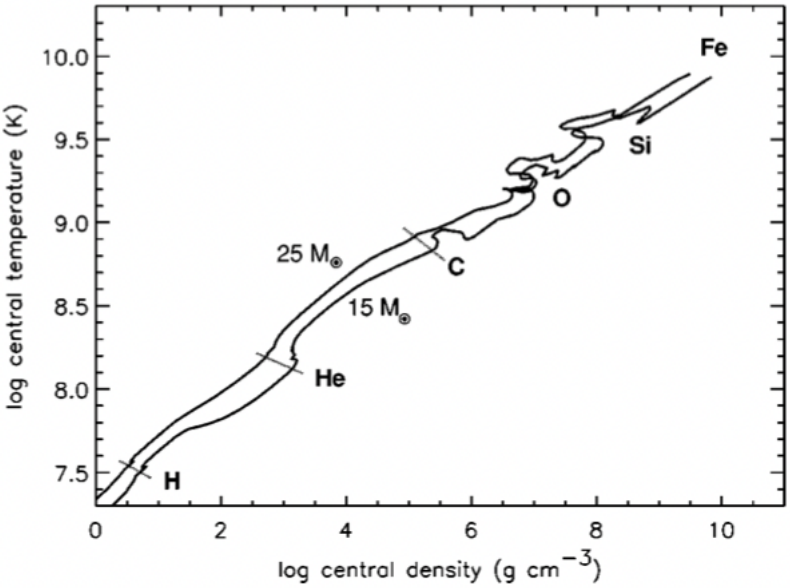

Figure 3.1: Evolution of central temperature and density in stars of $15\,M_\odot$ and $25\,M_\odot$. Image of Woosley et al. [2002]

or so [Clayton, 1983]. In fact, in these stages the luminosity of the nucleus is dominated by neutrino emission $L_\nu \sim \dot{E}_{nuc} = L_{nuc}$, where L_υ is the neutrino luminosity from the core, E_{nuc} is the nuclear energy the dot represent the time variation; L_{nuc} is the nuclear luminosity. The nuclear timescale is then obtained as:

$$\tau_{nuc} = \frac{E_{nuc}}{\dot{E}_{nuc}} = \frac{E_{nuc}}{L_\nu} \ll \frac{E_{nuc}}{L} \tag{3.2}$$

and it is much shorter than if neutrino losses were absent (L). The effect of neutrinos is even clearer when looking at figure 3.1. In general trajectories follows $\rho \propto T^3$, but, since carbon burning, the deviations are caused by the emission of thermal neutrinos.

The sequence of burning phases ends when the core is converted into iron. Each fusion process that leads to the formation of iron is exothermic because at each stage the binding energy of the system increases. But iron has the most stable of all nuclear configurations, so fusion of nuclei heavier than Fe would be endothermic and does not occur in nature. At this point the star is composed of a degenerate Fe core and different layers corresponding to the burning phases. Dynamical instability leads to the collapse of the core over its own gravity. It is the beginning of core-collapse supernova process, described in section 3.3.2, which will result in the formation of a compact object (NS or BH) depending on the final mass of the progenitor star.

3.2 Binary stellar evolution

Evolution of a star may change when it is in a binary system. If the orbit of the binary is wide enough, stars evolve as if they were without a companion (detached binary). Otherwise, if the binary is tight enough, it will evolve through several processes which might significantly change its final fate.

Wind mass transfer

In a binary, stars can exchange each other matter going through the so called mass transfer episodes. This can manifest via stellar winds or Roche lobe overflow. A star can accrete material from the companion in case the latter manifests mass loss due to stellar wind. The mean mass accretion rate can be estimated according to Hurley et al. [2002], based on Bondi and Hoyle [1944] formalism:

$$\dot{m}_2 = -\frac{1}{\sqrt{1-e^2}}\left(\frac{Gm_2}{v_w^2}\right)^2 \frac{\alpha_w}{2a^2}\frac{1}{(1+v^2)^{\frac{3}{2}}}\dot{m}_1 \tag{3.3}$$

where $\dot{m}_2$ is the mass accretion rate of the secondary, e is the eccentricity, G is the gravitational constant, v_w is the wind velocity, α_w is an efficiency constant, a is the semi-major axis of the binary, $\dot{m}_1$ is the mass loss rate of the primary and v^2 is equal to:

$$v^2 = \frac{v_{\text{orb}}^2}{v_w^2} \tag{3.4}$$

and

$$v_{\text{orb}} = \sqrt{\frac{G(m_1+m2)}{a}} \tag{3.5}$$

Since typically $\dot{m}_1 < 10^{-3}\, M_\odot \text{yr}^{-1}$ and the wind velocity is quite high ($> 1000\, km\, s^{-1}$ for a line driven wind) with respect to the orbital velocity, this kind of mass transfer is usually inefficient [Mapelli, 2022].

Roche-lobe mass transfer

The other possible mass transfer mechanism is Roche lobe overflow. The Roche lobe of a star in a binary is a drop-like equipotential surface that surrounds the star. Eggleton [1983] provide the approximation for the radius of the Roche lobe for the primary:

$$r_{L,1} = a\frac{0.49q^{2/3}}{0.6q^{2/3} + \log(1+q^{1/3})} \tag{3.6}$$

where a is the semi-major axis of the binary and $q = m_1/m_2$ is the mass ratio. One can obtain the radius for the secondary star just by swapping m_1 and m_2. The intersection point between the Roche lobes of the two stars is called *Lagrangian point* L_1. When a star fills its Roche lobe part of its mass is transferred to the other through L_1 as shown in figure 3.2. Mass transfer obviously changes the mass of the two stars in a binary, and thus

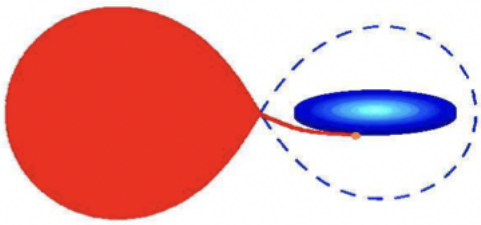

Figure 3.2: Cartoon of Roche lobe overflow mass transfer. Image of Podsiadlowski [2014]

the final mass of the compact remnants of such stars, but also the orbital properties of the binary. Mass transfer is usually non conservative and this leads to angular momentum loss, which in turn reduces the orbital eccentricity circularizing the orbit. Mass transfer is stable if the primary overfills its own Roche lobe. If also the secondary fills its Roche lobe then the mass transfer is unstable and a *contact binary* is formed. In this scenario, the typical subsequent process is the so called *common envelope*.

Common envelope

When two stars enter ~~in~~ a common envelope (CE) phase, their envelopes stop co-rotating with the core and form a unique envelope which embeds the cores. Their orbital energy decreases due to friction with the material of the envelope, which heats up and becomes more loosely bound. If the envelope is ejected, the post-CE binary is composed of two naked cores. Moreover their orbital separation is extremely smaller than the initial orbital separation before CE. This particular scenario is really helpful to form BBHs that are going to merge within Hubble time. In fact, assumed that both stars evolves and becomes black holes, the BBH will have a short semi-major axis ($a \lesssim 100\,R_\odot$) which allows to enter into the inspiral phase due to GW emission. If instead the envelope is not ejected, the cores spiral in till they eventually merge. This prevents the system to become a BBH.

The most common formalism for common envelope is the $\alpha\lambda$ formalism. In practice it uses the loss orbital energy as the only energy needed to eject the envelope.

$$\alpha \Delta E_{\rm orb} = \alpha \frac{G m_{c1} m_{c2}}{2} \left(\frac{1}{a_f} - \frac{1}{a_i} \right) = \frac{E_{\rm bind}}{\lambda}, \tag{3.7}$$

where $\Delta E_{\rm orb}$ is the difference between the orbital binding energy before and after CE phase, a_i and a_f are the semi-major axis before and after the CE phase, m_{c1} and m_{c2} are the masses of the cores, α is a dimensionless parameter that measures which fraction of the removed orbital energy is transferred to the envelope and λ measures the mass distribution of the envelope.

The binding energy of the envelope is:

$$E_{\rm env} = \frac{G}{\lambda} \left(\frac{m_{\rm env,1} m_1}{R_1} + \frac{m_{\rm env,2} m_2}{R_2} \right) \tag{3.8}$$

where m_1 and m_2 are the masses of the binary members, $m_{\rm env,1}$ and $m_{\rm env,2}$ are the envelope masses, R_1 and R_2 are the radii of the members. The higher is α, the more efficient is the energy transfer to the envelope and the higher is the probability for the binary to survive the CE phase.

GW emission

If the system successfully expels the envelop than two naked core stars remain in a tight orbit. Peters [1964] showed that a binary system is induced to merge because of GW emission. In fact there is an expression that connects the time variation of the semi-major axis with the GW emission:

$$\frac{da}{dt} = -\frac{64}{5} \frac{G^3 m_1 m_2 (m_1 + m_2)}{c^5 (1 - e^2)^{\frac{7}{2}}} a^{-3} \tag{3.9}$$

where c is the speed of light. This equation implies that the more eccentric the binary is, the faster the system will merge due to GW emission.

3.3 Supernova classification

The final fate of a star's life mainly depends on its mass. There are different possible explosion scenarios which will now be presented.

The current scheme of supernova classification includes numerous supernova types and sub-types defined according to observational properties, mostly visible-light spectra near maximum light, as well as photometric properties. The two main groups of supernova events are: Type-I, which have no observable hydrogen lines; Type-II which do have strong hydrogen lines.

Type Ia

Type Ia supernovae have a spectrum that contains neither hydrogen nor helium lines. It is dominated by absorption lines from intermediate-mass elements, and in particular it shows a very prominent silicon II absorption line. These supernovae are thermonuclear explosion of a carbon oxygen white dwarf in a binary system. There are two main progenitors competing scenarios to explain Type Ia supernovae: single-degenerate and double-degenerate model. In the single-degenerate case, a CO white dwarf accretes material from its non-degenerate companion star, which typically is a main-sequence or a red giant star. As more material is accreted, the central temperature increases, the mass reaches the Chandrasekhar limit and a runaway explosion is triggered. In the double-degenerate scenario a binary-white dwarf system coalesce due to gravitational wave emission. In this picture the merger product is represented by massive white dwarf accreting materials from an envelope and an accretion disk. If the white dwarf can evolve to the Chandrasekhar mass limit, then the system would undergo a runaway thermonuclear explosion. Type-Ia are the only supernova type which is not caused by the collapse of the iron core [Hillebrandt and Niemeyer, 2000, Maeda and Terada, 2016].

3.3.1 Core collapse supernovae observations

All the remaining supernova types and subtypes of supernovae come essentially from the same process, the collapse of the iron core in an evolved massive star. Before presenting the physical mechanism of core collapse, in the following sections we will see other two subcategories of Type I and the four groups of Type II supernovae. These, as previously mentioned, all contain strong hydrogen lines in their spectra.

Type Ib and Ic

Like Type Ia, they do not show hydrogen lines in their spectra. Type Ib show a strong He I absorption line, while Type Ic supernovae do not. It is possible to assume that Type Ib originate from the core collapse of a Wolf-Rayet star which has lost all its hydrogen envelope. Similarly, progenitors of Type Ic supernovae have lost also the helium envelope.

Type IIP

Above all the Type II supernovae, they are the most abundant component being the 70% of all [Li et al., 2011]. They can be distinguished from other subtypes by the presence, in the light curve, of a plateau lasting for the first 60-100 days followed by a sharp drop in luminosity. Progenitors of these supernova type are identified to be red supergiants with large hydrogen envelopes [Smartt et al., 2009].

Type IIn

These supernovae have narrow emission lines in their spectra. Type IIn are thought to arise from the interaction between the supernova expanding shock wave and the dense circumstellar medium, which is surrounding the explosion because it was previously expelled by the star itself through mass loss episodes. Ionisation of the surrounding circumstellar material results in an excess of narrow Hα lines. Spectra present also broad line components which are due to fast moving ejecta ($v \gtrsim 100$km/s) [Ransome et al., 2021]. Type IIn accounts for the 7% of all the Type II supernovae [Li et al., 2011].

Type IIb

Type IIb progenitors are massive stars which have lost almost all their hydrogen envelope. In fact, in the early phases, spectra show evident Balmer lines which are soon replaced by He I lines. At this stage the spectra resemble the ones of Type Ib supernovae, making these a transitional type between Type II and Type Ib. They account for 17% of all Type II supernovae.

Type IIL

They are characterized by the linear uninterrupted decline of the light curve and a lack of a prominent plateau phase. This is believed to be caused by the expulsion of most of the hydrogen envelope of the progenitor star before the explosion takes place [Doggett and Branch, 1985]. They are about 10% of all Type II supernovae [Li et al., 2011].

3.3.2 Theory of core-collapse supernova

At the end of the hydrostatic burning, a massive star ($M \gtrsim 10\,M_\odot$) consists of a degenerate iron core and a series of concentric shells that are the relics of its previous burning phases (hydrogen, helium, carbon, neon, oxygen, silicon). When the iron core grows by silicon shell burning to a mass around the Chandrasekar mass limit (about $1.44\,M_\odot$ [Chandrasekhar, 1931]), electron degeneracy pressure can no longer stabilize the core and it collapses. In the early stages of the collapse, the fraction of electron decreases due to electron capture. It consists in a reaction between a proton and an electron, to form a neutron with the emission of an electron neutrino.

$$p + e^- \rightarrow n + \nu_e$$

This decreases the electron degeneracy pressure accelerating the collapse. Also, photodisintegration takes place in the core. Due to high temperature, very energetic photons are produced that tend to destroy heavy nuclei into alpha particles, reversing the process of fusion. This removes thermal energy that would otherwise be supporting the core.

The collapse is strongly accelerated and an important change in the physics of the mechanism occurs when the density reaches $\rho_{\rm trap} \sim 10^{12}\, g\, cm^{-3}$. At this point neutrinos are trapped in the core, because their diffusion time becomes longer than the collapse time. The collapse continue until nuclear densities are reached ($\rho_0 \sim 10^{14} g\, cm^{-3}$). Neutrons become degenerate and the equation of state (EoS) becomes stiff. Nuclear matter has much lower compressibility, so the core decelerates and bounces in response to the increased nuclear matter pressure. The shock wave propagates into the outer core, which is the region that is still falling inwards at supersonic speed. This shock has not enough energy to drive the explosion, so it is used to dissociate heavy nuclei of the outer core into nucleons. This change in composition results in even more energy loss, because the electron capture rate on free protons is significantly larger than on neutron-rich nuclei. Huge amount of neutrinos are then produced behind the shock, which leave the star quickly with the so called neutrino burst. The shock is weakened so much that it finally stalls at a radius between $100 - 200$ km. Meanwhile a compact remnant begins to form at the center of the collapsing star. The proto-neutron star is initially still proton-rich and contains a large number of electrons and neutrinos. The latter are trapped because their mean-free path is comparable with the size of the core. It takes a fraction of second to the trapped neutrinos to diffuse out [Burrows, 1990]. The interactions between these highly energetic neutrinos and the other particles heats up the stellar medium in the region between the nascent neutron star and the stalled shock. This neutrino heating increases the pressure behind the shock creating a "hot bubble" between the shock and the proto-NS. The persistent energy input by neutrinos drives the shock outwards again, leading to a successful explosion. It is called "delayed neutrino-heating mechanism" [Janka et al., 2007] and usually takes a few 100 ms and requires that a few percent of the radiated neutrino energy are converted to thermal energy of nucleons, leptons, and photons.

Hardly any other astrophysical event is as complex and physically diverse as the death of massive stars in a gravitational collapse and subsequent supernova explosion. All four fundamental forces of nature take place and have important role in extreme regimes conditions. The study of these phenomena is usually done through hydrodynamical simulations. The CCSN models implemented in the SEVN code are usually taken from hydrodynamical studies of the collapse and explosion mechanism.

3.3.3 Electron-capture supernova (ECSN) observations

ECSNe are the primary candidates to explain some transients showing luminosity between classical novae ($M_v \sim -8$) and supernova explosions ($M_v \sim -17$) [Cai et al., 2019]. Within this gap, a fraction of these transients are called "supernova impostors" as they mimic some observational properties of H-rich interacting supernovae, but deep late-time imaging reveals that the progenitor stars survived [Van Dyk et al., 2000]. Their typical peak absolute magnitudes are between -13 and -15 mag. Giant eruptions of luminous blue variables are considered a plausible interpretation for classical supernova impostors.

Another class of gap transient has double peaked light curves and fast evolving spectra. They are conventionally named as "luminous red novae" [Cai et al., 2019]. This phenomenon is usually interpreted as a post common envelope ejections phase in a contact binary system and may be followed by stellar coalescence [Pastorello et al., 2019].

The third group of gap transients are named intermediate luminosity red transients (ILRTs) [Pastorello and Fraser, 2019]. These show a slow rise time (~ 2 weeks) to maximum ($-11\,\text{mag} < M_v < -14.5\,\text{mag}$), followed by a linear decline lasting about 2-4 months. The origin of these transients remains mysterious, but ECSNe are plausible

candidates to explain this scenario. ECSNe are predicted to display distinctive features: luminous super-AGB progenitors ($\sim 10^5\,L_\odot$) [Poelarends et al., 2008], low explosion energies ($\sim 10^{50}$erg) and low ejected ^{56}Ni mass (few $10^{-3}M_\odot$). The rate of observations of these events is strongly dependent on the initial mass range, metallicity, and the details of the stellar model. There have been some estimates of the ILRT rate compared with CCSN rate, for example: Cai et al. [2021] found that, over a volume with radius 30 Mpc, the rate of ILRTs is 8% of that of CCSNe; Thompson et al. [2009] found ECSN rate of $2\% - 10\%$ of CCSNe in ten years before 2008. It is difficult to estimate the degree of uncertainty on such numbers because surveys, up to 30 Mpc, are incomplete.

3.3.4 Electron-capture supernova theory

Stars with initial masses between 8 and 10 $M_\odot$ have an interesting transition from massive white dwarf (WD) formation to core collapse supernova. In fact they are thought to form a degenerate oxygen-neon-magnesium (O-Ne-Mg) core through non explosive carbon burning. These objects are labelled as "Super-AGB stars" and their fate is uncertain due to the many complications involved in modelling their interiors and evolution, especially regarding the role of mixing, convective overshooting and mass loss rates. Whether super-AGB stars evolve in a O-Ne-Mg WD or undergo core collapse through electron capture is still being investigated [Doherty et al., 2017]. Electron capture becomes very important when we are dealing with a strongly degenerate O-Ne-Mg cores. In fact, when the core mass grows to $1.38M_\odot$ due to shell burning, and the central density reaches $2\times10^9\,\mathrm{g\,cm^{-3}}$, electron capture on Mg and Ne isotopes should lead to dynamical instability and therefore collapse of the core, inducing what is called electron capture supernova. The structure of the O-Ne-Mg core is distinctively different from the iron cores of more massive stars by the fact that it has a steep density gradient in the outermost layers, surrounded by an extremely extended, loosely bound H/He envelope [Wanajo et al., 2009].

3.3.5 Pair instability and pulsational pair instability supernovae

Pair-instability supernovae (PISNe) are theorized supernovae that have not yet been observationally confirmed. They are thought to exist in low metallicity environments. The overall metallicity becomes lower at higher redshift, which means that near-infrared, high redshift surveys may be able to find PISN events [Moriya et al., 2019].

PISNe comes from thermonuclear explosions of very massive stars and they are predicted to produce a large amount of radioactive ^{56}Ni that heats supernova ejecta, increasing the luminosity of the explosion. They were firstly associated with supernova events which are more than 10 times more luminous then otheer supernovae, known as superluminous supernovae (SLSNe) [Gal-Yam, 2019]. However, the light curve and the spectral properties of SLSNe are now found to be different from those predicted for PISNe [Mazzali et al., 2019]. Revealing PISN events would be fundamental in order to test stellar evolution, chemical evolution and mass distribution of BHs observed by GWs.

Physycs of the explosion

The core of very massive stars with initial masses higher than about $100\,M_\odot$ [Heger et al., 2003] has relatively low density and high temperatures for which radiation pressure is dominant over gas pressure. When the core temperature reaches $10^9\,K$, the creation of electron-positron pairs out of gamma-ray photons from the high energy tail of the black

body spectrum becomes important. Dynamical instability of the core is controlled by the adiabatic index:

$$\gamma_{\rm ad} = \left(\frac{\partial \log P}{\partial \log \rho}\right)_{\rm ad} \tag{3.10}$$

when it falls below 4/3 dynamical instability occurs and the gravitational collapse of the core begins.

When this instability is encountered, the star contracts rapidly until implosive oxygen and silicon burning, depending on the mass of the star, produce enough energy to revert the collapse and completely disrupts the star if the released energy exceeds its binding energy. For a pair instability supernova to occur, its progenitor needs to retain its mass high enough to keep its helium core mass above about $\sim 65\,M_\odot$. This condition cannot be easily fulfilled at high metallicity for which the evolution of very massive stars are dominated by stellar wind mass-loss [Vink et al., 2011]. This requirement on the mass of the star is set by the minimum temperature and density conditions in the core for the pair instability to occur. On the other hand there is an upper limit on the Helium core mass of the star $M_{\rm He} \lesssim 133\,M_\odot$. It corresponds to the case when all the energy generated in the explosive burning is equal to the binding energy of the star. Above this limit, the infall is not reversed into an explosion and the star directly collapses to a BH.

If, instead, the amount of released nuclear energy is less than the binding energy of the star, a fraction of the envelope may be ejected. After such an eruption, the star relaxes to hydrostatic conditions on a thermal timescale. If the remaining stellar mass is sufficiently high for pair creation, the star undergoes a second pair creation episode accompanied by another eruption. This phenomena is the so called pulsational pair instability. It occurs typically for stars with $100 < M_{\rm ZAMS}/M_\odot \lesssim 140$. After the sequence of eruptions a star may not be anymore able to undergo pair creation episodes. So it continue its evolution as a massive star, typically ending its life as a BH.

Chapter 4

Methods

4.1 SEVN

SEVN (Stellar EVolution for N-body) is a population synthesis code which calculates stellar evolution by interpolating a set of pre-computed stellar tracks [Spera et al., 2019]. It includes binary evolution by means of analytic and semi-analytic prescriptions for wind mass transfer, Roche lobe overflow, common envelope phase, gravitational waves emission. To perform the interpolation, in SEVN the lifetime of a star is divided into different stellar phases as shown in 4.1 and the final remnant is listed as Table 4.2.

Phase int	Phase string	Physics
0	PreMainSequence	
1	MainSequence	Core H-burning start
2	TerminalMainSequence	Creation of a He core
3	HshellBurning	He core almost formed
4	HecoreBurning	Core He-burning start
5	TerminalHecoreBurning	Creation of a CO core
6	HeshellBurning	CO core almost formed
7	Remnant	Star is dead

Table 4.1: List of integer values used for stellar evolution phases.

RemType int	RemType string	Physics
0	NotARemnant	Star is not a remnant
1	HeWD	Helium White-Dwarf
2	COWD	CO White-Dwarf
3	ONeWD	Oxygen-Neon White-Dwarf
4	NS_{ECSN}	NS after ElectroCapture SN
5	NS_{CCSN}	NS after Core Collapse SN
6	BH	Black Hole
-1	Empty	Massless remnant

Table 4.2: List of integer values used for remnant types.

4.1.1 Stellar tracks

The default stellar tracks of SEVN are computed with the stellar evolutionary code `PARSEC` [Bressan et al., 2012]. These tables contain the information on star mass, star radius, core radius, stellar metallicity and evolutionary stages. The metallicity and mass ranges for these stellar tracks are $Z = 10^{-4} \div 4 \cdot 10^{-2}$ and $2.2 \leq M_{ZAMS}/M_{\odot} \leq 600$. In addition SEVN includes a set of tracks for bare Helium cores to describe the evolution of stars which lose their whole hydrogen envelope after mass transfer phase. For these tables the metallicity and mass ranges are: $Z = 10^{-4} \div 5 \cdot 10^{-2}$, $0.36 \leq M_{\mathrm{He}_{ZAMS}}/M_{\odot} \leq 350$.

4.1.2 Core collapse supernova models

SEVN includes different models to describe the outcome of a CCSN event. In my thesis I have compared three of them: rapid, delayed and compactness model.

Rapid

The rapid model, described by Fryer et al. [2012] and implemented in Spera et al. [2019], assumes that the explosions either occurs quickly within 250 ms after the core bounce or not at all. With this model, the final mass of a compact object and the type of remnant depend on the CO core mass M_{CO} at the time of core bounce/explosion and on the final mass of the star M. The proto-compact object mass is set to: $M_{proto} = 1\,M_{\odot}$. Depending on the amount of mass above the proto-compact object $(M - M_{proto})$ and the strength of the explosion, the potential fallback may increase the compact object mass. The final bayonic mass of the remnant is then calculated as:

$$M_{rem,bar} = M_{proto} + M_{fb} \tag{4.1}$$

M_{fb} is the fallback mass and it is defined as:

$$M_{fb} = f_{fb}\,(M - M_{proto}) \tag{4.2}$$

with f_{fb} being the fractional fallback parameter defined in [Fryer et al., 2012, equation 16], which describes the fraction of material that falls back on the compact object. It depends on the CO core mass and when $M_{CO} > 11 M_{\odot}$ the fractional fallback parameter is equal to 1 and the CCSN mechanism ends with a direct collapse (BH formation).

Delayed

The delayed model is also described in Fryer et al. [2012] but in this case the SN explosion can occur over a much longer timescale and includes a certain amount of fallback. Again the final remnant mass is obtained with equation (4.1). The differences with the rapid model lie in the amount of fallback [Fryer et al., 2012, equation 19]. Also in this case, when the CO core mass is bigger than $11 M_{\odot}$, the model predicts a direct collapse.

Compactness

The compactness model is based on the compactness parameter, defined as:

$$\xi_{2.5} = \left.\frac{M/M_{\odot}}{R(M_{\mathrm{bary}} = M)/1000\,km}\right|_{t=t_{bounce}} \tag{4.3}$$

with $M = 2.5 M_\odot$ and R being the radial coordinate that encloses a mass equal to M at the time of core bounce [O'Connor and Ott, 2011]. The evaluation of $\xi_{2.5}$ at core bounce is crucial, since this is the only physical and unambiguous point in core collapse at which one can define a zero of time and can describe the true initial conditions for postbounce evolution. In SEVN, the compactness is estimated using the fitting formula of Mapelli et al. [2020], where $\xi_{2.5}$ monotonically increases as the CO mass at the onset of collapse grows:

$$\xi_{2.5} = a + b \left(\frac{M_{CO}}{1\, M_\odot} \right)^c \tag{4.4}$$

with $a = 0.55$, $b = -1.1$, $c = -1.0$ It is possible to define a compactness threshold ξ_t so that small compactness values ($\xi_{2.5} \leq \xi_t$) produce a supernova explosion, while when $\xi_{2.5} > \xi_t$ a BH is formed by direct collapse. In SEVN the default value for the threshold is $\xi_{2.5} = 0.35$. There is still no a single certain value of the compactness threshold: O'Connor and Ott [2011] suggested that progenitors with $\xi_{2.5} > 0.45$ most likely form BHs, while Horiuchi et al. [2014] used $\xi_t = 0.2$ and Mapelli et al. [2020] adopted $\xi_t = 0.3$. In my thesis I run simulations with five different compactness thresholds: $\xi_t = [0.1, 0.2, 0.3, 0.4, 0.5]$.

When the progenitor explodes leaving a NS, the mass of the NS is assigned randomly following a gaussian distribution with mean $\langle M_{NS} \rangle = 1.33\, M_\odot$ and dispersion $\sigma = 0.09\, M_\odot$ based on the distribution of binary NS systems of Özel and Freire [2016].

When the progenitor undergoes direct collapse the mass of the BH is obtained as:

$$M_{BH} = M_{He} + f_H \left(M_{fin} - M_{He} \right) \tag{4.5}$$

where M_{He} is the mass of the He core at the onset of collapse, M_{fin} is the total final mass at the onset of collapse, f_H is a free parameter which can take values from 0 to 1 and it accounts for the fraction of hydrogen envelope that collapses. In my simulations f_H is fixed to 0.9.

4.1.3 Pair instability and pulsational pair instability

The new version of SEVN includes two main models to describe PPIs and PISNe: M20 and F19.

M20 is the same model implemented in Mapelli et al. [2020] based on Woosley [2017]. If He-core mass is in the range $64 \leq m_{\rm He}/M_\odot \leq 135$, the star undergoes PISN leaving no remnant. If the He-core mass lies in $32 \leq m_{\rm He}/M_\odot < 64$ the star undergoes pulsational pair instability and the final mass of the compact object is calculated with the following formula:

$$m_{\rm rem} = \alpha_P\, m_{\rm no\ PPI} \tag{4.6}$$

with $m_{\rm no\ PPI}$ being the mass predicted by the adopted core-collapse supernova model and α_P fitting parameter (see Equation 4 and 5 in the Appendix of Mapelli et al. [2020]).

F19 is based on MESA simulations of pure-He core stars made by Farmer et al. [2019]. They find that at the highest metallicities stellar winds also remove all the remainging helium from the star, starting to eject C/O rich materials in the pre-pulses. For this reason they use the CO core mass over the He core mass as a better proxy for the activation of PPISN and PISN. The defined limits for the instability regions are: $38 < M_{CO}/M_\odot < 60$ for PPISN; $M_{CO} > 60\, M_\odot$ for PISN (see figure 2 of Farmer et al. [2019]). The mass of the

BHs that form after pulsational pair-instability are estimated using the fitting formula:

$$M_{\rm BH} = \begin{cases} 4 + M_{\rm CO} & M_{\rm CO} < 38 \\ a_1 M_{\rm CO}^2 + a_2 M_{\rm CO} + a_3 \log_{10}(Z) + a_4 & 38 \leqslant M_{\rm CO} \leqslant 60 \\ 0.0 & M_{\rm CO} > 60 \end{cases} \tag{4.7}$$

where Z is the metallicity, $a_1 = -0.096$, $a_2 = 8.654$, $a_3 = -2.07$, $a_4 = -152.97$ and all masses are in units of $M_\odot$. In general, for F19, SEVN derives the mass of the compact remnant as:

$$m_{\rm rem,PPISN} = \min(M_f,\, M_{F19}) \tag{4.8}$$

where M_f is the pre-supernova mass of the exploding star and M_{F19} is the BH mass of equation (4.7).

In both models is assumed that a PISN explosion leaves no compact remnants.

4.1.4 Initial conditions

In my simulations of binary stellar evolution the initial conditions consist in a set of 10^6 binary systems with fixed metallicity. The primary stars are generated in the range $[5, 150]\, M_\odot$ following a Kroupa initial mass function (IMF) [Kroupa, 2001]:

$$p(m) = k\, m^{-\alpha} \tag{4.9}$$

$$\alpha = 1.35 \text{ for } m < 0.8 \tag{4.10}$$

$$\alpha = 2.35 \text{ for } m > 0.8 \tag{4.11}$$

where k is the normalization constant. The proportion between the part of Kroupa that I am using and the one missing in my IMF gives a factor of 0.285 which will multiply the BH population obtained with the simulations.

Secondary stars are generated assuming a distribution of mass ratios from Sana et al. [2012]:

$$\text{pdf}(q) \propto q^{-0.1} \qquad q = \frac{M_2}{M_1} \in [0.1, 1.0]\, M_\odot \tag{4.12}$$

For single stellar evolution I have done the same procedure, but generating single stars following a Kroupa distribution in the range $[10, 150] M_\odot$. Here I am not interested in having all the domain filled, I just want to have a visual comparison between single and binary stellar evolution. In figure 4.1 is shown the IMF used for binary and single stellar evolution. SSE strictly follows the Kroupa mass function, while in BSE the little deviation is caused by the presence of secondary stars, which are the ones that fill the range of masses below $5\, M_\odot$.

In all my simulations I use a set of 14 metallicities: $Z = [10^{-4}, 2 \times 10^{-4}, 4 \times 10^{-4}, 6 \times 10^{-4}, 8 \times 10^{-4}, 10^{-3}, 2 \times 10^{-3}, 4 \times 10^{-3}, 6 \times 10^{-3}, 8 \times 10^{-3}, 10^{-2}, 1.4 \times 10^{-2}, 1.7 \times 10^{-2}, 2 \times 10^{-2}]$.

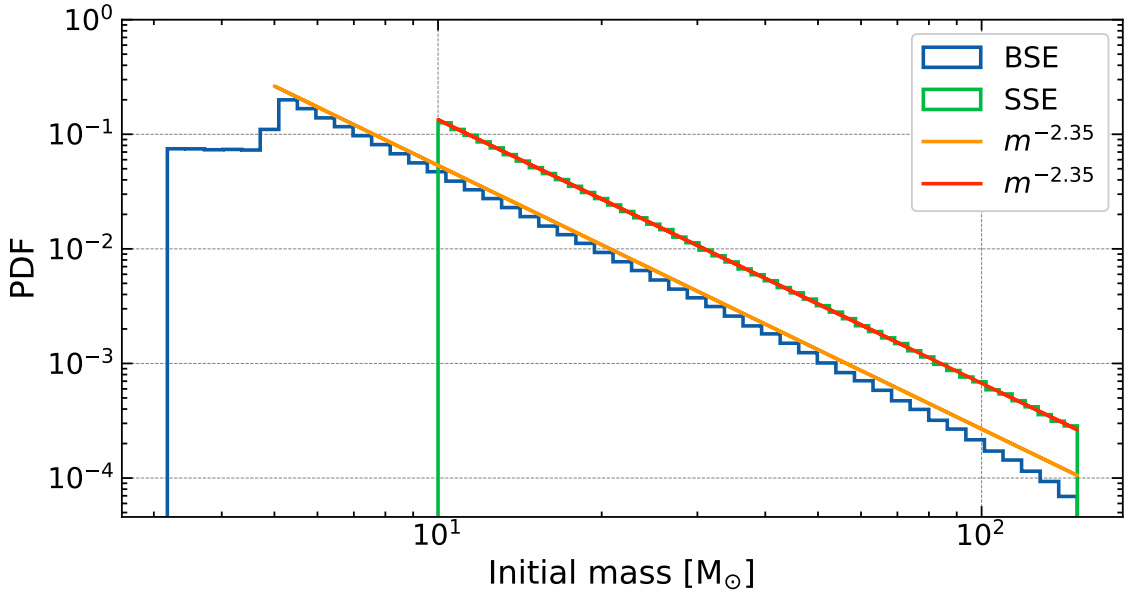

Figure 4.1: Initial mass function for binary stellar evolution (Blue) and single stellar evolution (Green) with the theoretical trend in orange and red.

Chapter 5

Results

5.1 Single star evolution (SSE)

Figure 5.1 shows the mass spectrum of black holes that are formed after the evolution of an initial population of single stars. The two columns are obtained using M20 and F19 model for pair-instability, respectively (4.1.3). We take into account six metallicity values, that cover all the range from metal-poor to metal-rich stars. This figure shows how sensitive the maximum mass of the BH and the PISN window are to the details of stellar evolution. The first thing to notice is the role of metallicity on stellar evolution. Metallicity is a key parameter that controls many aspects of the formation and the evolution of both stars and galaxies, one of which is the mass loss through stellar winds [Leitherer et al., 1992, Vink et al., 2001]. When metallicity increases, a star tends to lose more mass through stellar winds and the evolution will lead to a lighter compact remnant. A clear example of this can be seen for both M20 and F19 (top left and right panels of figure 5.1), where at $Z = 0.02$ the mass of the produced BHs reaches at most $25\,M_\odot$ with the heaviest ZAMS star. For lower metallicities, $Z = 10^{-3} \div 10^{-4}$, at ZAMS masses between $30M_\odot$ and $60M_\odot$, the BHs almost follow the bisector, which means that the progenitor star did not lose much mass during its life. For $Z < 10^{-2}$ the spectra are characterized by sharp oscillations because the PPISN region has been reached (figure 5.1 bottom panels). In M20, when a star has a pre-supernova He-core mass between $37\,M_\odot$ and $64\,M_\odot$, it enters the pulsational pair-instability range (between $32M_\odot$ and $37\,M_\odot$ PPISN is not very efficient) and the final remnant mass decreases. This is clear looking at $Z = 10^{-4}$: at $M_{zams} \sim 60\,M_\odot$, the corresponding He-core mass is above the lower limit for pulsational pair instability. This translates into a steep decrease in the mass of the BHs. The same happens for the F19 model, but at higher masses. As visible in the bottom-right panel of this figure, at $Z = 10^{-4}$, the lower edge of pulsational pair instability ($M_{CO} = 38\,M_\odot$) corresponds to a ZAMS mass $M_{zams} \sim 80\,M_\odot$ and the BH mass steeply drops from values of $\sim 80\,M_\odot$ to $\sim 40\,M_\odot$.

The non-monotonic trend of CO-core and He-core mass is due to the dredge-up events that take place in several stellar models of the tables (4.1.1). Dredge-up occurs during the evolution of a star when the convective outer layers penetrate down to the core. The fusion products are then brought up to the surface and mixed in the outer layers of the star, reducing the mass of the core. This can be seen by looking how the He(CO)-core mass varies around $M_{zams} = 80\,M_\odot$ and the consequent variation of the final mass of the BH.

In some cases, dredge-up may enhance the formation of high mass black holes. If

$M_{zams} \sim 100\,M_\odot$ and $Z = 10^{-4}$, the decrease of M_{He} and M_{CO} caused by the dredge-up allows the star to avoid PPISN, producing a BH with masses up to $90\,M_\odot$ for M20 and $100\,M_\odot$ for F19.

Going to higher ZAMS masses, almost all the tracks reach the pulsational pair-instability regime in different points, depending on the metallicity. For $M_{zams} \gtrsim 80\,M_\odot$ the BH mass is determined using equation (4.6) for M20 and (4.8) for F19, which give the mass of the BH that forms from CCSN, having gone through a phase of pulsational pair instability. This happens also for masses $\sim 150\,M_\odot$ at metallicity $Z = 10^{-4}$.

In this Figure, we adopted the rapid CCSN model, but our previous discussion on pulsational pair instability and pair instability is applicable to all the other models we have taken into account. Figure 5.2, 5.3, 5.4, 5.5 show the same mass spectra presented in figure 5.1 but with, respectively, delayed and compactness model with threshold at $\xi_t = 0.1, 0.3, 0.5$. The trends above all the models are very similar for both M20 and F19. There are, however, some clear differences between the different CCSN models adopted. Comparing rapid and delayed (figures 5.1 and 5.2), the main difference between the two is in the lightest BH produced. In the rapid model, there are no BHs below $5\,M_\odot$ and in general no compact remnant between $2\,M_\odot$ and $5\,M_\odot$. It mimics the lower mass gap that we also have from observations: a dearth of compact objects has been seen in that range, where the lower limit corresponds to the heaviest NS. The delayed model, instead, does not present any gaps, allowing to form BHs down to $3\,M_\odot$, which corresponds also to the highest mass value for a NS to form.

Compactness models [O'Connor and Ott, 2011] present a slightly different trend for low ZAMS masses (at least in $\xi_t = 0.1$ and $\xi_t = 0.3$), with respect to Fryer et al. [2012] models (rapid and delayed). Independently of metallicity, all the tracks stay on the bisector until stellar winds become important (earlier for higher metallicities. See figures 5.3-5.5). This happens because, for the compactness model, the parameter for the fractional fallback is fixed to 0.9. For rapid and delayed, instead, the fractional fallback f_{fb} depends on the pre-supernova CO mass and it is defined following equation 16 of Fryer et al. [2012].

Now, comparing the three compactness thresholds, they differ only in the lower edge of the spectrum. Higher ξ_t requires higher initial mass in order to form a BH and indeed while the lightest BH for $\xi_t = 0.1$ has a mass around $5\,M_\odot$, it reaches $\sim 25\,M_\odot$ when $\xi_t = 0.5$. With the highest compactness threshold (figure 5.5) there are no BHs formed with metallicity $Z = 0.02$. At this metallicity, stars at the end of their evolution tend to be less massive due to strong stellar winds and their final mass is not sufficiently high to produce a compactness value bigger than the threshold.

5.1.1 Discussion

The most important thing that can be learned from these figures is that the mass distribution of BHs is extremely sensitive to the PISN model used. Woosley [2017] and Farmer et al. [2019] both do hydrodynamical simulations together with stellar evolution. They are able to describe the physics of the explosions, for example estimating the amount of mass lost during pulsations in a PPISN. SEVN, instead, can not do hydrodynamics, so the details in the mass spectra must be taken as an indicative trend. The role of dredge-up in this context is crucial and can determine whether a star goes completely disrupted through PISN, or avoid that, falling in PPISN regime and forming a BH or else whether it undergoes PPISN or it enters in the stable region of CCSNe.

Therefore, these trends, obtained for single stars, help to understand the effect that certain models or parameter might have on stellar evolution and consequently on the

populations of compact objects, in this case BHs, that are produced.

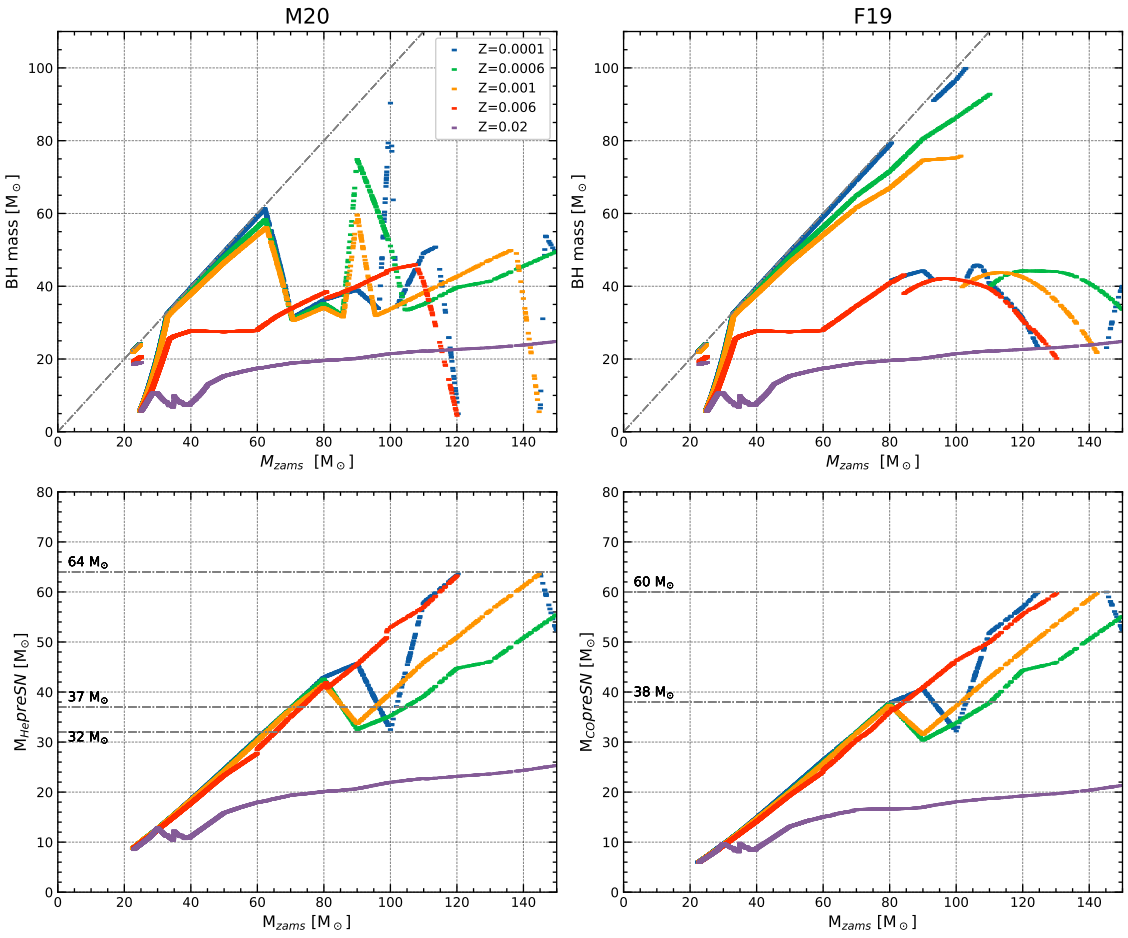

Figure 5.1: BH and pre-supernova mass as a function of ZAMS mass from single stellar evolution. The left-hand column is obtained using the pair-instability model M20 based on Mapelli et al. [2020]; the right-hand column is obtained using the pair-instability model F19 based on Farmer et al. [2019]. In both cases I adopted the *rapid* core collapse supernova model (4.1.2). The bottom panels, from left to right, show the pre-supernova mass of the He core M_{He} and the CO core M_{CO}. In the model M20 the star is expected to undergo pulsational pair instability in the range $32 < M_{He}/M_{\odot} < 64$ (for $M_{He} > 37$ PPISN becomes more effective), while for $M_{He} > 64\,M_{\odot}$ the star is completely disrupted by pair-instability supernova. With the other model, F19, a star enters in the pulsational pair-instability regime if $38 < M_{CO}/M_{\odot} < 60$. For masses bigger than $60\,M_{\odot}$ the star undergoes PISN leaving no remnant. Different lines indicate different metallicity: $Z = 0.0001$ blue line; $Z = 0.0006$ green line; $Z = 0.001$ orange line ; $Z = 0.006$ red line; $Z = 0.02$ purple line.

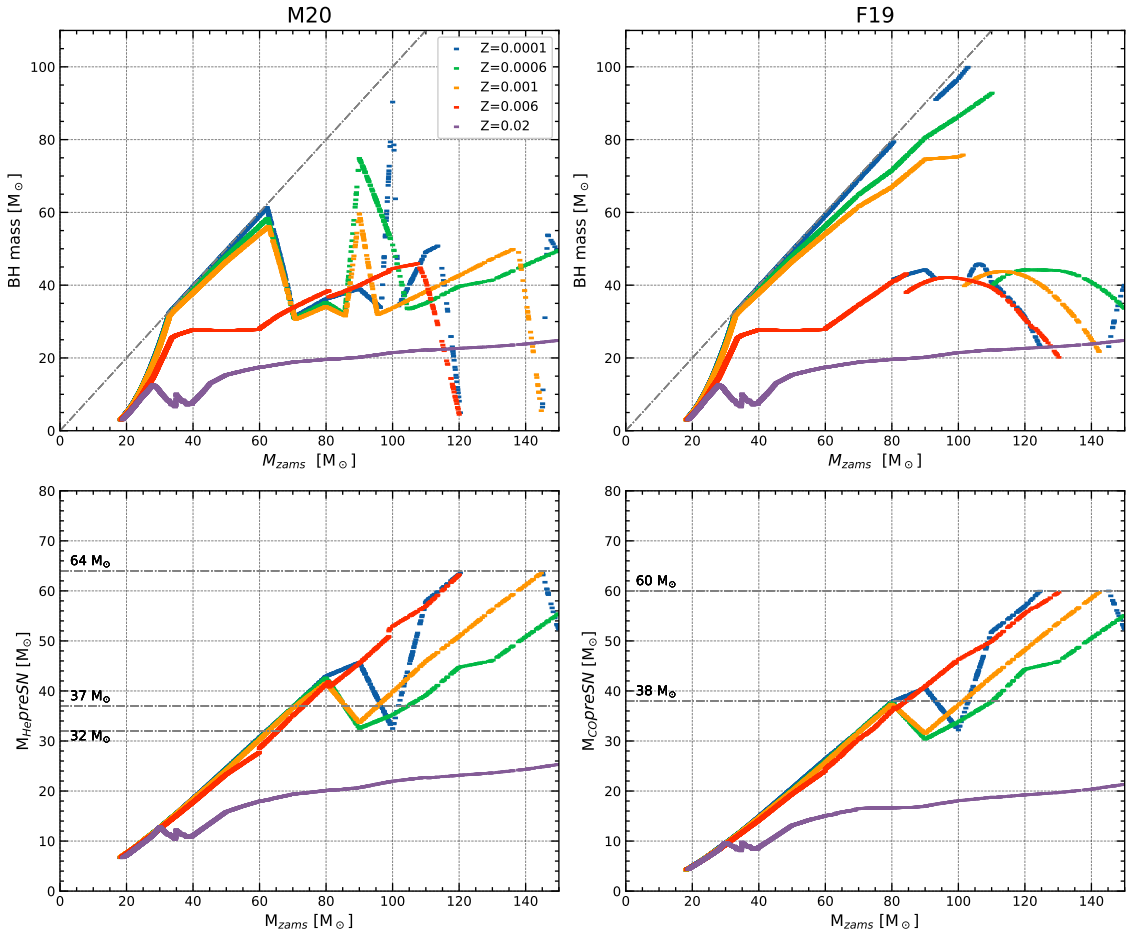

Figure 5.2: Same as figure 5.1 but with the *delayed* model for CCSN.

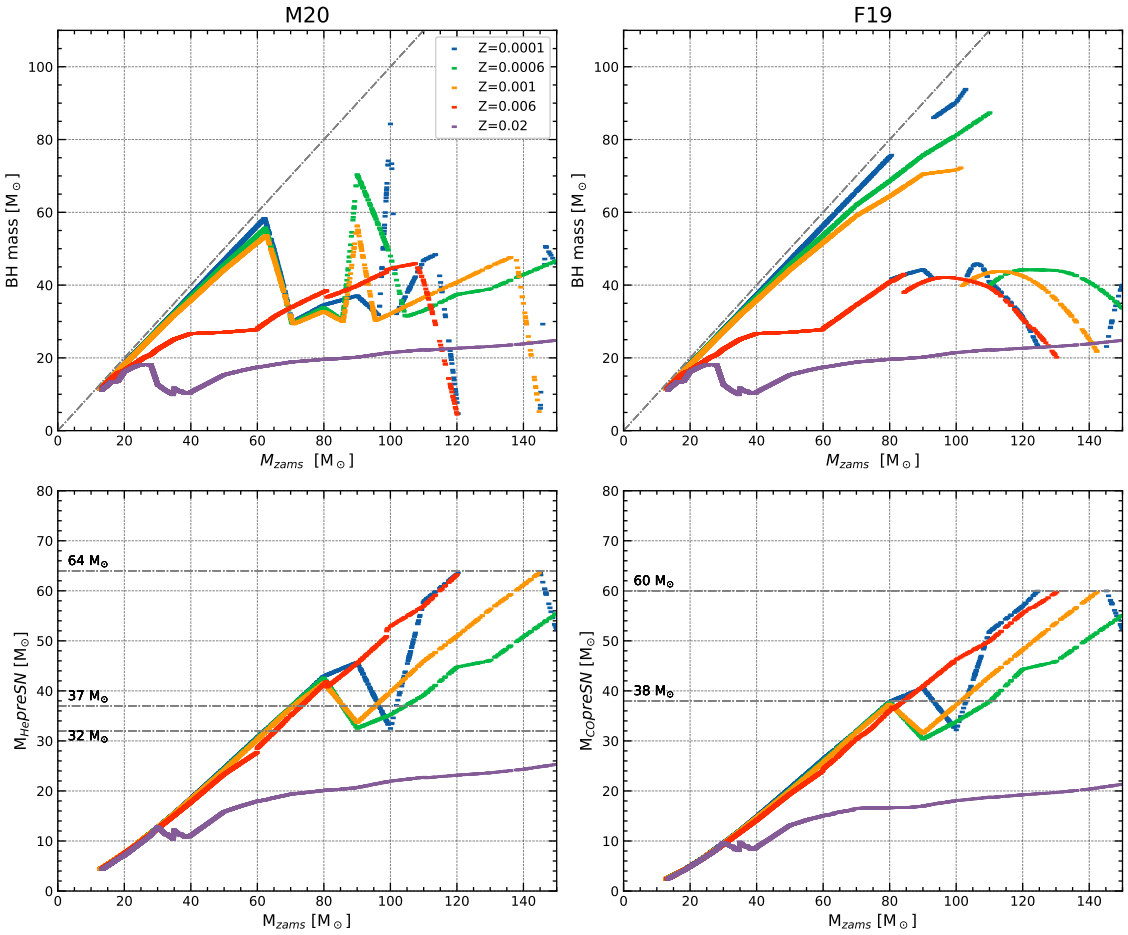

Figure 5.3: Same as figure 5.1 but with the *compactness* model for CCSN with the threshold of the compactness parameter fixed at $\xi_t = 0.1$.

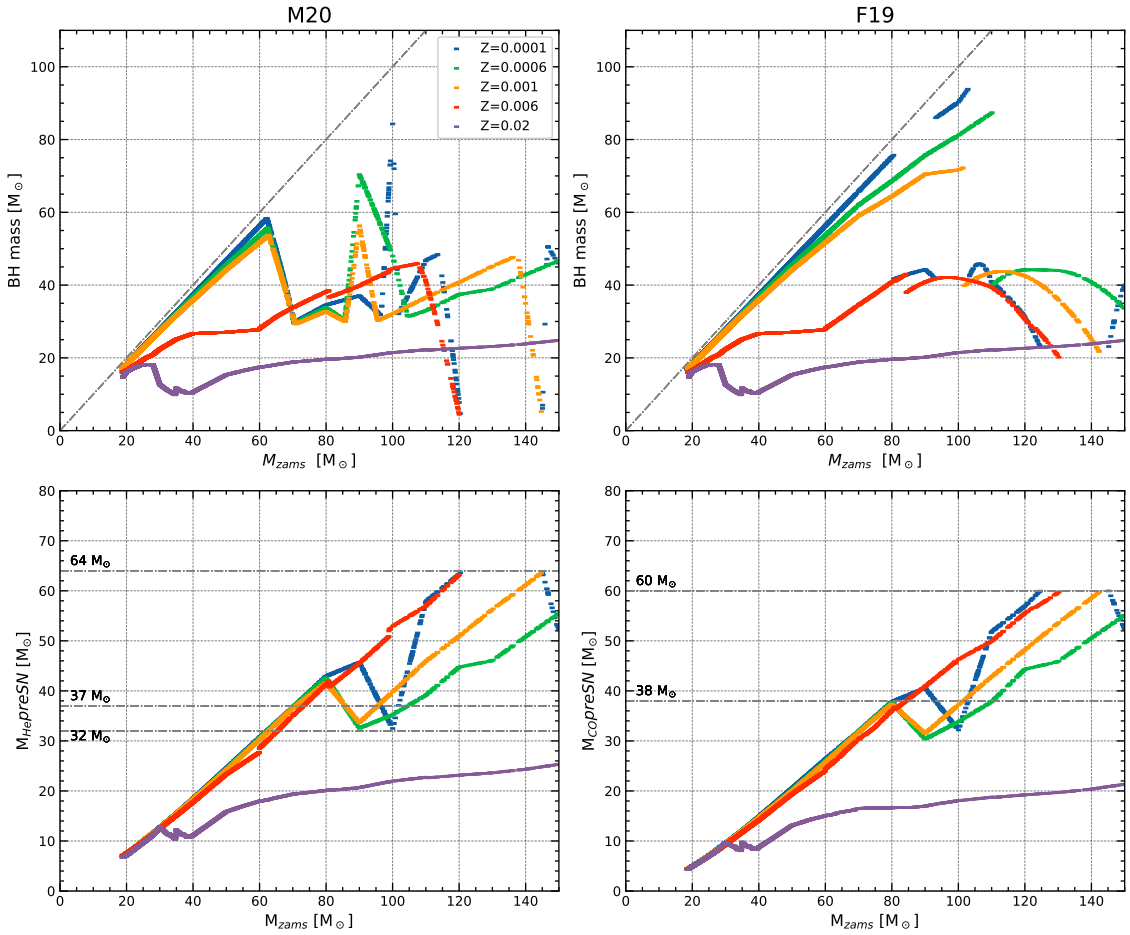

Figure 5.4: Same as figure 5.1 but with the *compactness* model for CCSN with the threshold of the compactness parameter fixed at $\xi_t = 0.3$.

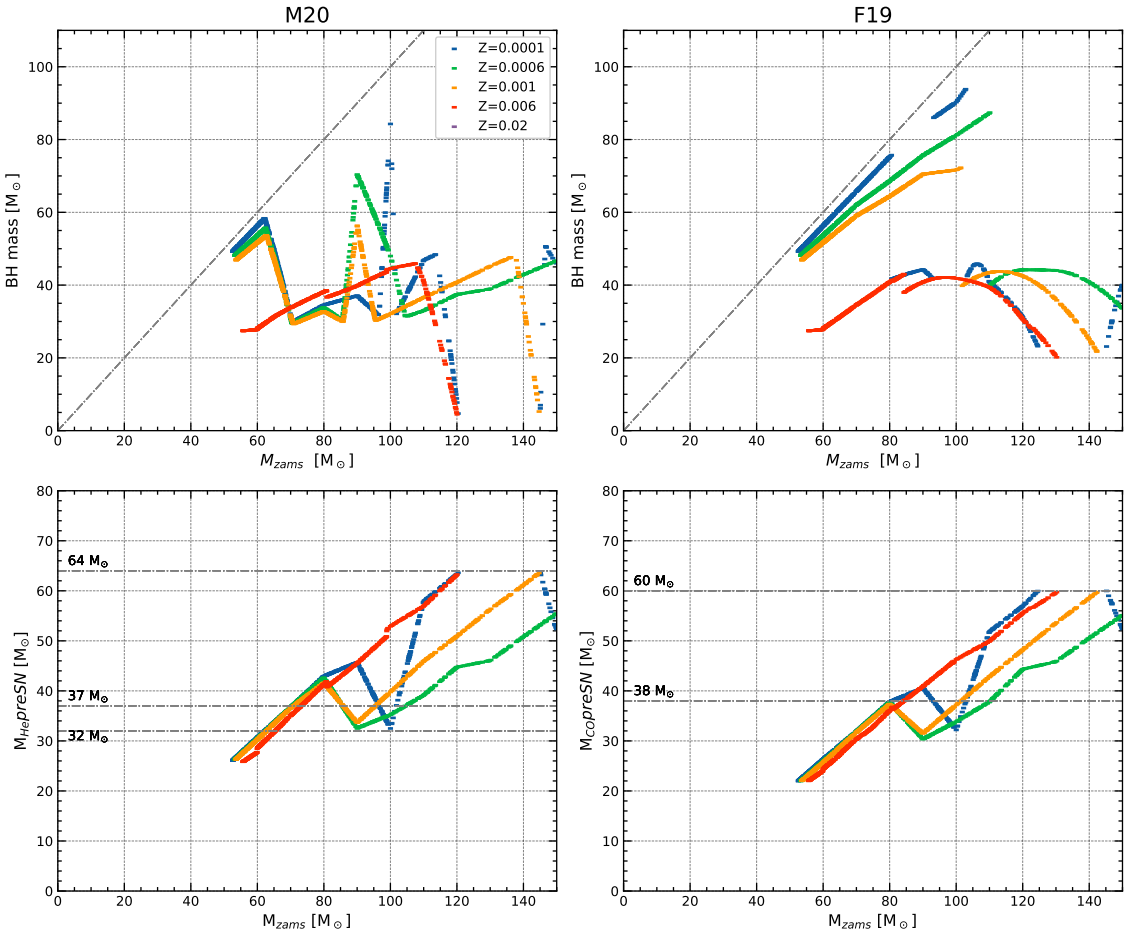

Figure 5.5: Same as figure 5.1 but with the *compactness* model for CCSN with the threshold of the compactness parameter fixed at $\xi_t = 0.5$.

5.2 Binary star evolution (BSE)

When dealing with binary evolution, SEVN takes into account the interaction between the components of the binary system, which can completely change the final fate of a star's life. Stars with a certain value of ZAMS mass may end their life producing a BH that is way more(less) massive with respect to the SSE case because they have accreted(donated) mass through mass transfer episodes.

Figure 5.6 shows the mass spectrum of all the BHs in binary systems produced after the simulation using the *rapid* CCSN model. The two columns represent the spectra obtained with PISN models M20 and F19. Different rows correspond to different metallicities and the red line superimposed to the image represent the track of SSE, the one described in the previous section. The red line is important to understand whether a star accreted mass and created a more massive BH, or else it donated mass, leaving a lighter compact remnant. For example, if we fix a final mass value $M_{rem} = 20\,M_{\odot}$, except for $Z = 0.02$, we see that a significant amount of BHs is present both above and below the red SSE line. BHs that are below the red track have a progenitor that donated mass, in fact they form a BH with the same mass but starting from a bigger initial mass, while, for the opposite reason, BHs above the red line are formed by an accretor star. In general, the majority of BHs that are located below the single stellar evolution curve come from primary stars (the heavier star on the zero-age main sequence in the binary system), while the region above the red curve is mostly populated by secondary stars. From figure 5.6 it also appears that most of most compact remnants distribute along the SSE curve.

The differences between M20 and F19 (left- and right-hand column) are the same already mentioned in the previous section. The heaviest black holes are always found along the single stellar evolution line for each model and for each metallicity. This is not surprising since primaries in binary systems go through mass transfer episodes, which means that in the best case scenario (detached binary) they evolve as if they were single stars. A comparison between BH masses obtained from binary and single stellar evolution is shown in Table 5.1 for M20 and 5.2 for F19. The maximum mass of BHs in loose binaries obtained from M20 and F19 is around $90\,M_{\odot}$ and $100\,M_{\odot}$, respectively.

In the following analysis, I will distinguish three populations of BHs:

1. all BHs in my simulations (hereafter, all BHs);

2. the sub-population of BHs that are members of BBHs at the end of my simulations (hereafter, bound BHs);

3. the sub-population of BHs that are members of BBHs that will merge within one Hubble time $t_{\rm H} = 14$ Gyr (hereafter, merging BHs).

Z	$M_{zams,\,min}$ SSE	$M_{zams,\,min}$ BSE	$M_{BH,max}$SSE	$M_{BH,max}$ BSE
10^{-4}	22.5 $M_{\odot}$	14.8 $M_{\odot}$	90.3$M_{\odot}$	90.7 $M_{\odot}$
6×10^{-4}	22.6 $M_{\odot}$	12.0 $M_{\odot}$	74.8 $M_{\odot}$	75.3$M_{\odot}$
1×10^{-3}	22.6 $M_{\odot}$	12.2 $M_{\odot}$	59.6 $M_{\odot}$	60.3 $M_{\odot}$
6×10^{-3}	22.8 $M_{\odot}$	8.6 $M_{\odot}$	45.9 $M_{\odot}$	47.6 $M_{\odot}$
2×10^{-2}	22.8 $M_{\odot}$	10.6 $M_{\odot}$	24.8 $M_{\odot}$	29.0 $M_{\odot}$

Table 5.1: Black hole and ZAMS masses with *rapid* and M20 models for CCSN and PISN respectively.

Z	$M_{zams,min}$ SSE	$M_{zams,min}$ BSE	$M_{BH,max}$SSE	$M_{BH,max}$ BSE
10^{-4}	22.5 $M_\odot$	14.8 $M_\odot$	99.9 $M_\odot$	100.1 $M_\odot$
6×10^{-4}	22.6 $M_\odot$	12.0 $M_\odot$	92.8 $M_\odot$	94.1 $M_\odot$
1×10^{-3}	22.6 $M_\odot$	12.2 $M_\odot$	75.8 $M_\odot$	78.8 $M_\odot$
6×10^{-3}	22.8 $M_\odot$	8.6 $M_\odot$	43.1 $M_\odot$	46.6 $M_\odot$
2×10^{-2}	22.7 $M_\odot$	10.9 $M_\odot$	24.8 $M_\odot$	29.0 $M_\odot$

Table 5.2: Black hole and ZAMS masses with *rapid* and F19 models for CCSN and PISN, respectively.

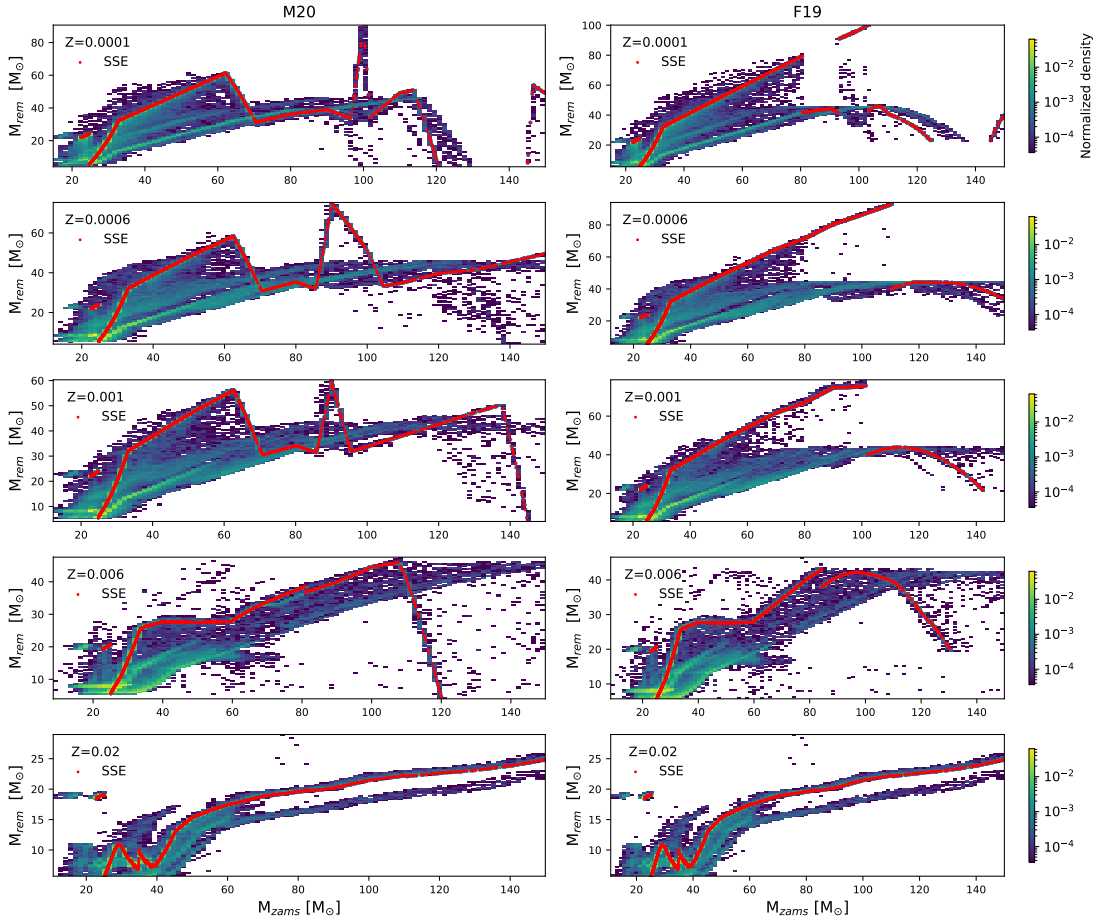

Figure 5.6: Mass of BHs ending up in compact-object binaries, as a function of the ZAMS mass of the progenitor star using *Rapid* CCSN model. The logarithmic colour bar represents the number of BHs per cell, normalized to the maximum cell-value of each plot. *Left-hand column* is obtained using M20 model for pair instability; *right-hand column* is obtained using F19 model for pair instability; each row shows the mass spectrum with a fixed metallicity of the initial population: $Z = 0.0001, 0.0006, 0.001, 0.006, 0.02$. The red curve represents the single-stellar evolution line.

In the following sections I show how the mass distribution of binary black holes changes as a function of the CCSN model.

5.2.1 Rapid and Delayed

Figure 5.7 shows the three sub-populations of BHs (all, bound and merging BHs) for all the considered metallicities.

The first row of this figure shows all the black holes produced during the simulation and it is complementary to figure 5.6. Indeed, we see clearly how many black holes there are for each value of their mass and it confirms what we have seen so far. The maximum black hole mass produced decreases with the metallicity going from around $90\,M_\odot$ for $Z = 10^{-4}$ to around $30, M_\odot$ for $Z = 10^{-2}$. Low metallicity also implies that a higher number of BHs are produced, because winds are quenched.

Bound black holes represent the vast majority of all the black holes produced and their mass distribution is nearly the same as the one of all black holes.

The big difference appears between the merging black holes (third row) and the other classes. The number of merging BHs drops significantly, reaching just few tens with the highest metallicity $Z = 0.02$. The tail of massive BHs present in the first two rows here disappears, leaving compact remnants with masses $< 60\,M_\odot$.

Figure 5.8 shows the mass distribution of black holes with delayed model and M20. The differences between rapid and delayed models are in the lower mass limit. By the definition given in Fryer et al. [2012], rapid corresponds to a fast-convection mechanism, in which explosions occur if they happen within 250 ms after bounce.

Delayed explosions, instead, can occur over a much longer timescale. In both cases the limit for supernova explosion energy is around a few times 10^{51} erg. Delayed explosions tend to be weaker than rapid ones, producing many more explosions at energies below 10^{51}erg (Fryer et al. [2012] figure 4). This broader range of energies allows the delayed mechanism to create a continuous range in remnant masses, while rapid explosion leads to a sharp transition between NSs and BHs. For this reason the lightest BH produced in the rapid scenario has mass around $5\,M_\odot$, while in delayed it reaches $\sim 3\,M_\odot$.

5.2.2 Compactness

Figure 5.9 shows the mass distribution of BHs with compactness and M20 models. This CCSN model is based on O'Connor and Ott [2011] compactness parameter $\xi_{2.5}$. In SEVN, the computation of $\xi_{2.5}$ is done with the fitting formula (4.4), that reproduces the strong correlation between compactness and CO mass found by [Limongi and Chieffi, 2018, figure 21], where $\xi_{2.5}$ monotonically increases with M_{CO}.

Each row of figure 5.9 shows the compactness threshold increasing from $\xi = 0.1$ to $\xi = 0.5$. As shown in the mass spectra for SSE (see figure 5.3, 5.4, 5.5), these models behave in the same way for large masses. That is true also in this binary case, in which, independently of the chosen threshold, the maximum mass for each model is nearly the same $\sim 83\,M_\odot$ at $Z = 10^{-4}$.

The main difference between rapid and delayed models, and compactness model is the minimum ZAMS mass required to form a BH. This difference manifests itself in the specific choice of compactness and we can see it with two examples: by inverting equation (4.4), with a threshold at $\xi_t = 0.1$, the corresponding CO mass is $M_{CO} = 2.4\,M_\odot$, while if $\xi_t = 0.5$ the required CO mass must be $M_{CO} = 22\,M_\odot$. It is clear that the minimum ZAMS mass necessary to form a BH is strongly correlated with the value of ξ_t. Increasing

the threshold also increases the minimum BH mass, and this can be perfectly seen by looking at figure 5.9 going from top to bottom row.

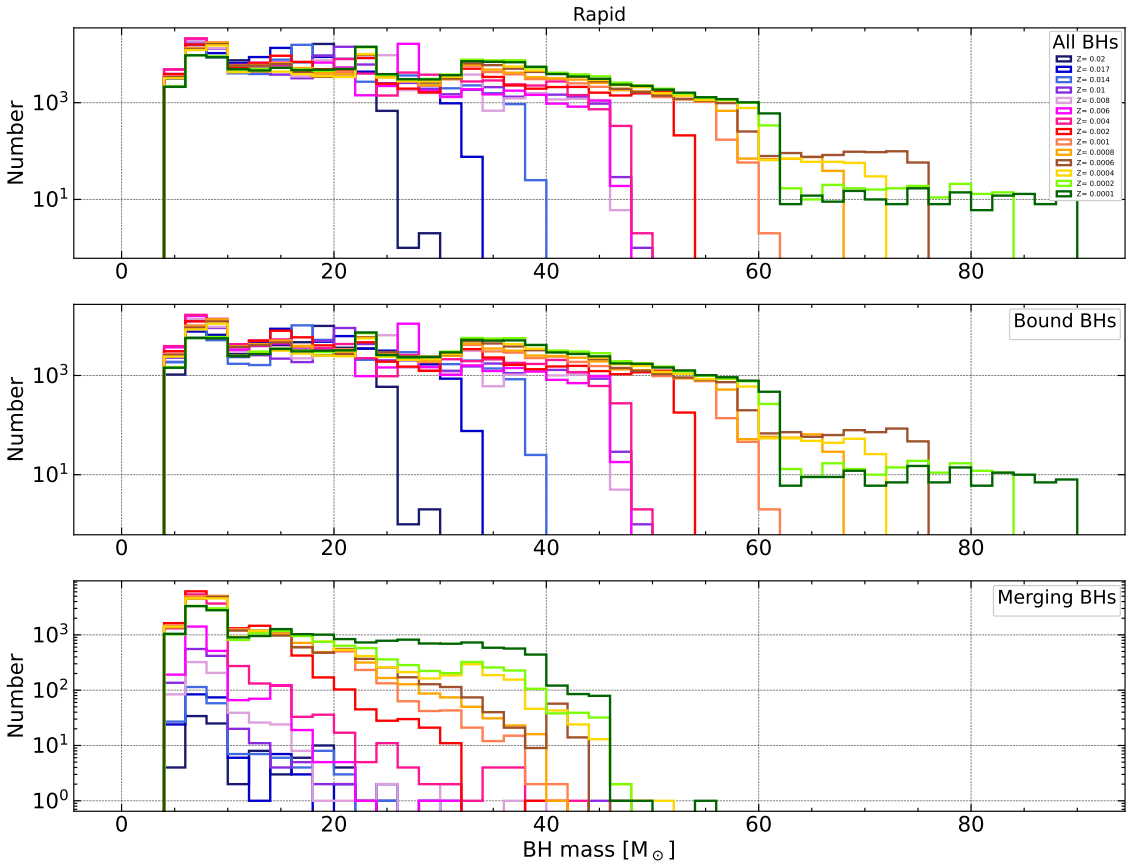

Figure 5.7: Mass distribution of black holes with different metallicity adopting the *rapid* and M20 models. The first row shows all black holes; the second row shows BHs in bound systems; the third row shows BHs which are going to merge within the Hubble time. Fourteen metallicities are taken into account ranging from 10^{-4} to 2×10^{-2}.

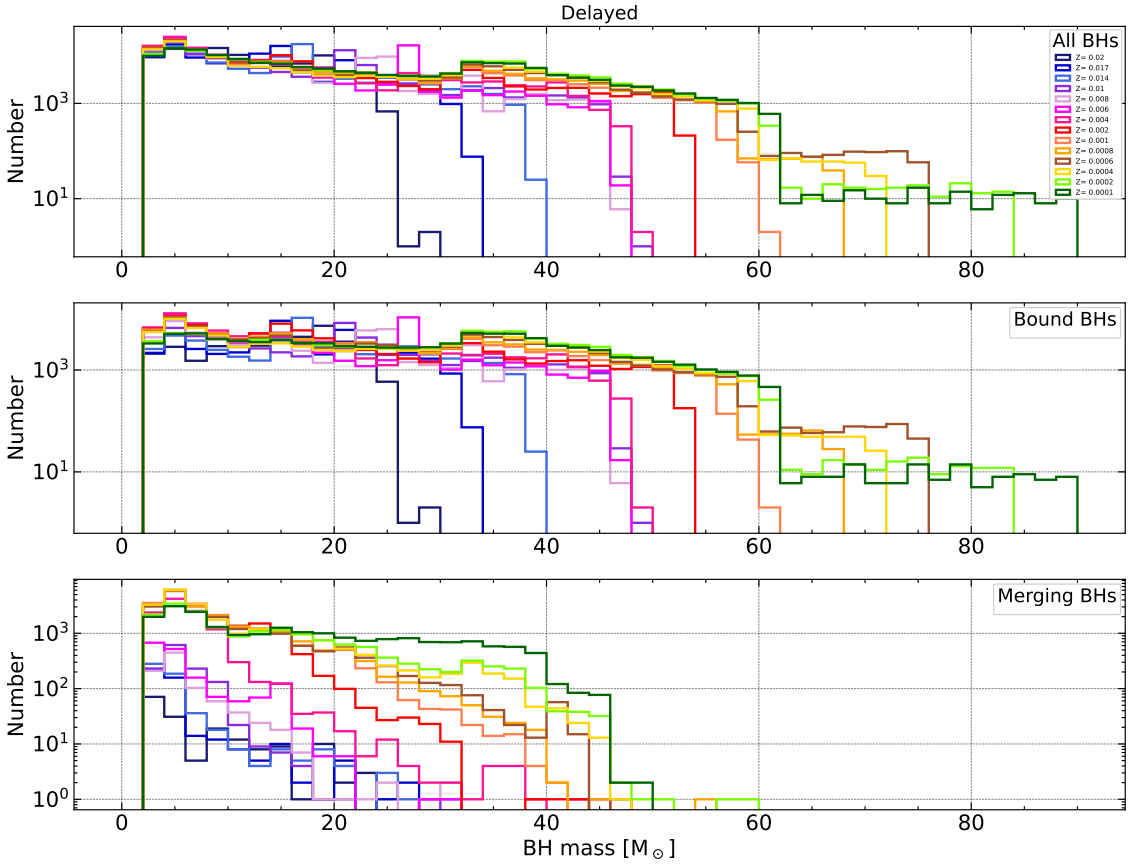

Figure 5.8: Mass distribution of black holes with different metallicities adopting the *delayed* and M20 models.

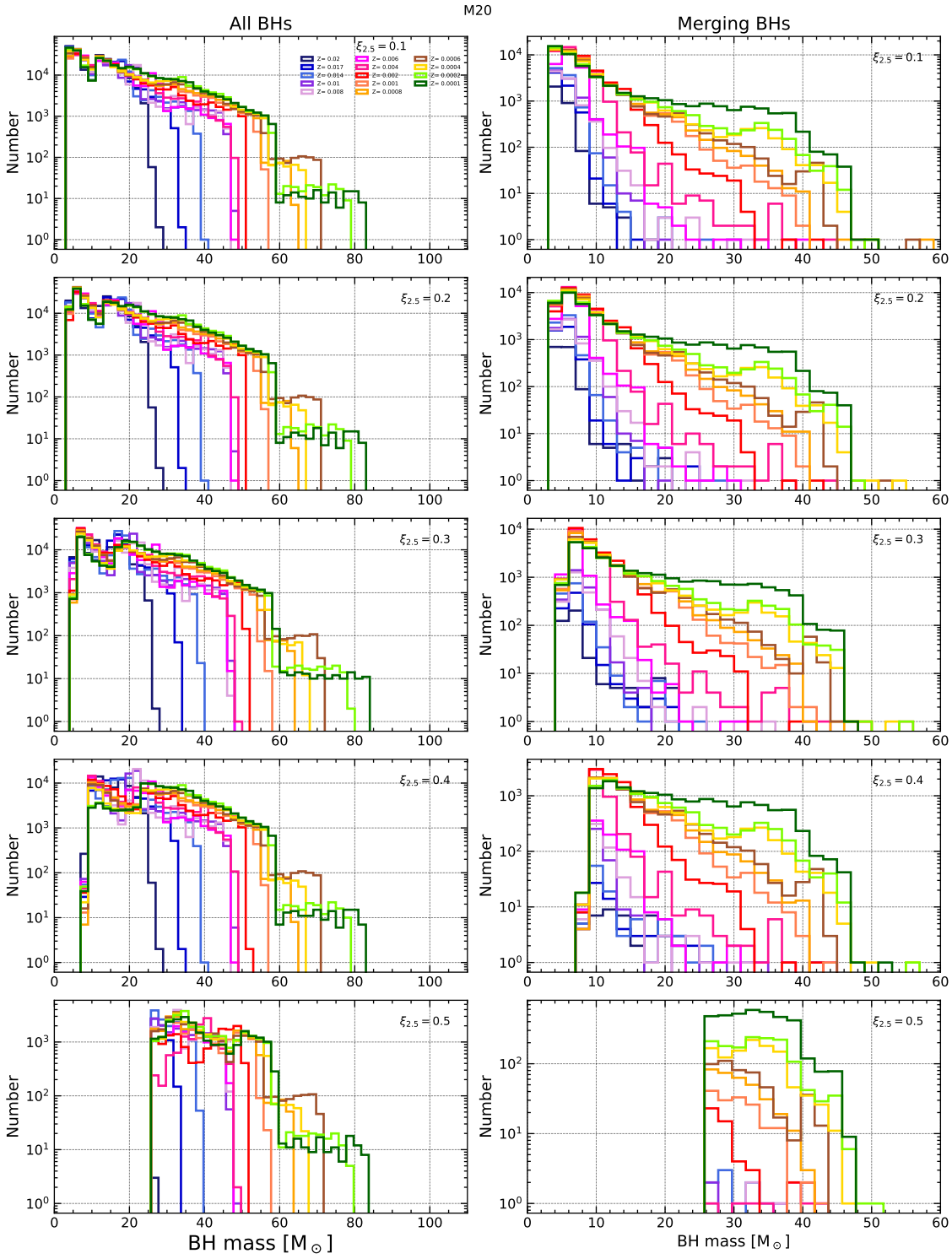

Figure 5.9: Mass distribution of black holes with different metallicities using *compactness* and M20 models. The left-hand column presents the complete population of black holes produced; the right-hand column shows the BBH systems which are going to merge within a Hubble time. Different rows corresponds to different compactness threshold from $\xi_t = 0.1$ to $\xi_t = 0.5$ with a step of 0.1. The metallicity varies in the range $10^{-4} \div 2 \times 10^{-2}$.

5.2.3 Supernova channels

One essential way to compare our results with the data is to quantify the incidence of different supernova types in our SEVN simulations with respect to the observations. The list of supernova types is reported in table 5.3. From my simulation, I extracted and compared the number CCSNe, ECSNe, PISNe and PPISNe. To count the number of pulsational and pair-instabilities for M20 we have to check if the final He-core mass falls inside the gap $32M_{\odot}-64M_{\odot}$, while for F19 the final CO-core mass must fall inside the gap $38M_{\odot} - 60M_{\odot}$. The number of CCSN BH/NS depends on the model. In the rapid and delayed models there is direct collapse (CCSN BH) when $M_{CO} > 11\,M_{\odot}$. If this condition is not satisfied, the event is classified as CCSN NS. With the compactness model, if $\xi_{2.5}$ at the pre-supernova stage (determined with (4.4)) is larger than ξ_t, then the event counts as a direct collapse (CCSN BH). If $\xi_{2.5} < \xi_t$ it counts as a CCSN NS.
ECSNe are independent of the CCSN model used.

From figure 5.10 to 5.16 we show the number of events as a function of the metallicity for al the CCSN models used, with M20. For the classification of the supernova types, it is also specified, in the case of CCSN, the type of remnant. Between rapid and delayed, the amount of all the possible supernovae is nearly the same. This is expected since they basically differ in the creation of low-mass black holes, which do not alter significantly the total number of direct collapses. For the compactness model the number of CCSN BHs decreases when the threshold becomes bigger. At the same time the number of CCSN NSs increases because those stars that previously formed a BH, start forming NSs when the threshold grows. Independently of the model, the number of CCSN events decreases when the metallicity increases. This is expected since at higher metallicity stellar winds become important decreasing the final mass of the star, reducing the possibility to form a NS or a BH.

The number of PISN and PPISN remains mostly the same for every model and for every compactness threshold. The reason for this can be found by looking at SSE tracks of figures 5.1-5.5 (left columns). While the low ZAMS mass range is strongly affected by the CCSN model choice, when we enter into the PPISN the spectra look almost the same. There are some deviations in the maximum BH masses, but the general behaviour for each mass spectrum is identical for each CCSN. As expected, the CCSN model does not affect the amount of PISN events, since they are determined by the pair-instability model chosen (M20 or F19).

The number of ECSNe can be compared with the number of CCSN events. We find that ECSNe are between 2% and 4% of all the CCSN events. These values can be compared with the observational results. Thompson et al. [2009] found, within a volume of 30Mpc, an observed ECSN rate of $2\% - 10\%$ of CCSNe. Cai et al. [2021] provide a rate of ILRTs within 30 Mpc is 8% of that of CCSNe. Our result is in the range found by Thompson et al. [2009], but the degree of uncertainty of these ratios is still difficult to estimate, because survey up to 30 Mpc are incomplete.

5.2.4 Discussion

The comparison between BSE and SSE gives a lot of information on the effects of interactions between binary components on the final mass of the compact objects (figures 5.1 and 5.6). The higher edge of the distribution is basically unchanged, because SSE scenarios may verify in a well-separated non interacting binary systems. In fact, black holes that originate from interacting binary systems tend to be smaller than single black

SN type Int	SN type str
0	Unknown
1	Electron Capture SN
2	Core Collapse SN
3	Pulsation Pair Instability SN (PPISN)
4	Pair Instability SN (PPISN)
5	la
6	WD

Table 5.3: Type of supernova mechanism and its correspondence integer reference number in SEVN.

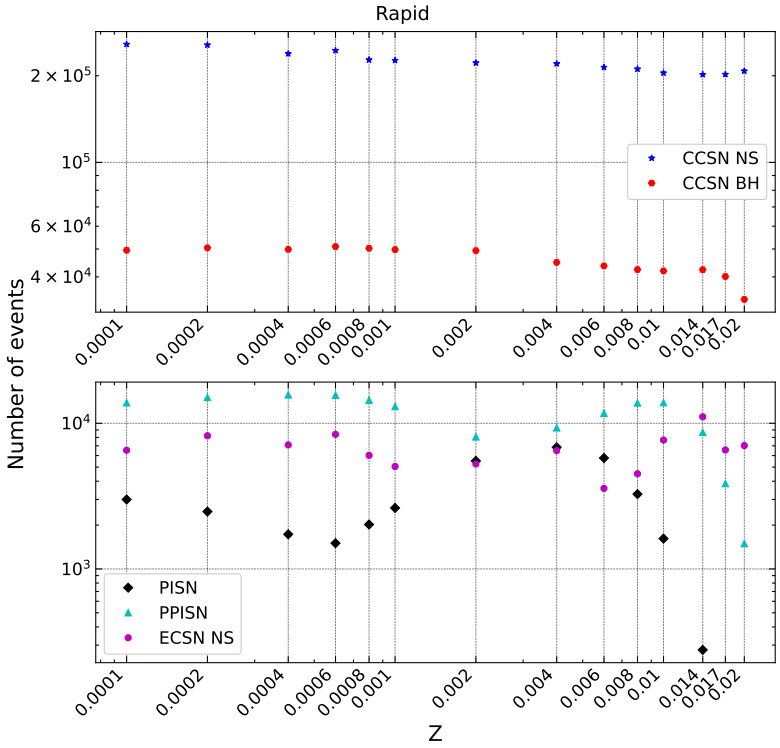

Figure 5.10: Number of supernova events divided per supernova type as a function of metallicity. *Rapid* (M20)

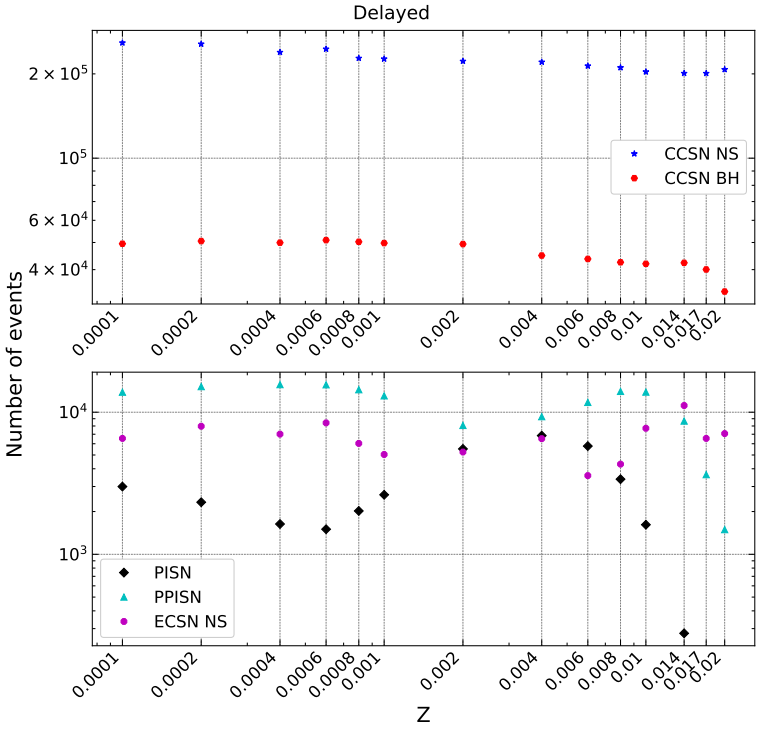

Figure 5.11: Same as Fig. 5.10, but for the *Delayed* (M20) model.

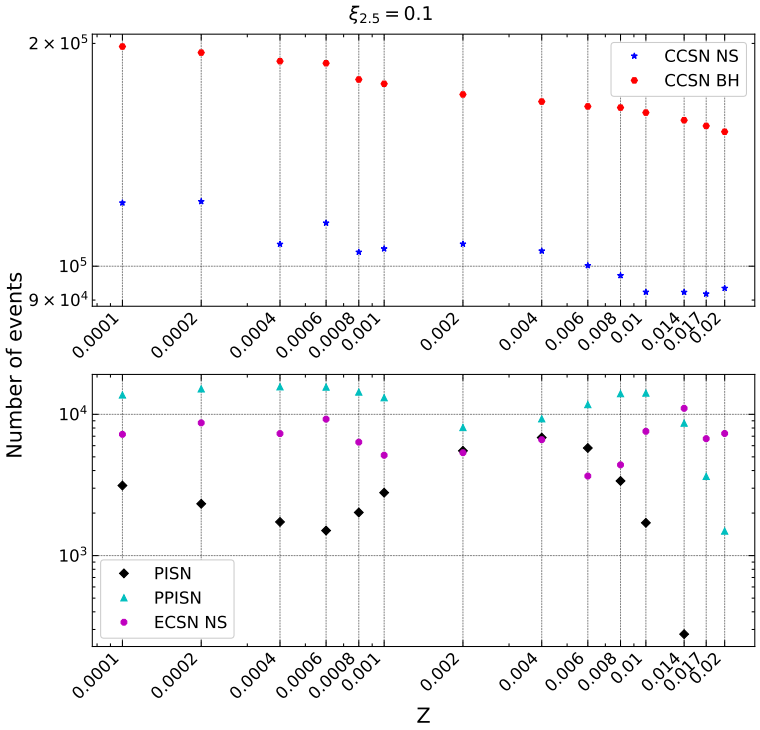

Figure 5.12: Same as Fig. 5.10, but for the *Compactness* model with $\xi_t = 0.1$ (M20).

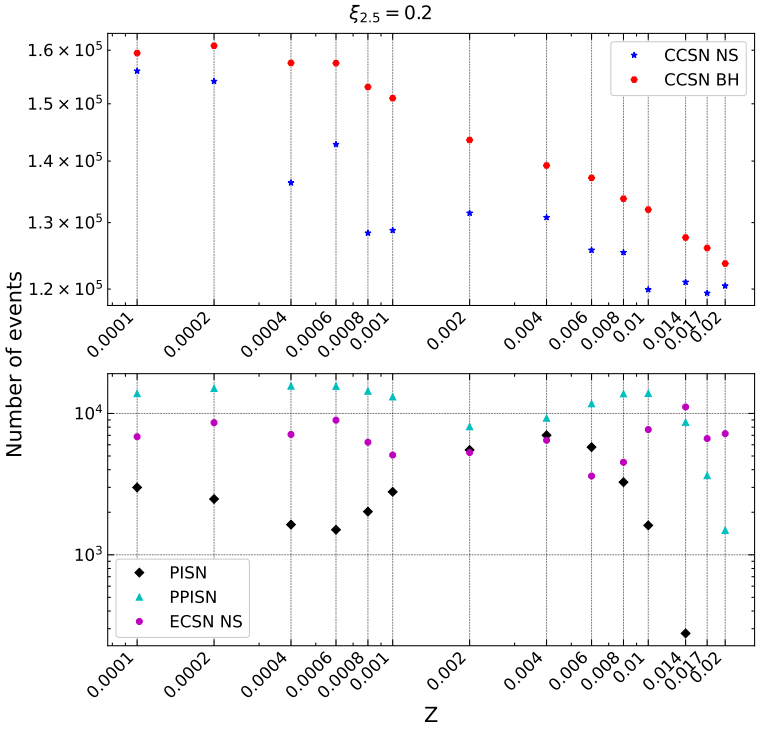

Figure 5.13: Same as Fig. 5.10, but for the *Compactness* model with $\xi_t = 0.2$ (M20).

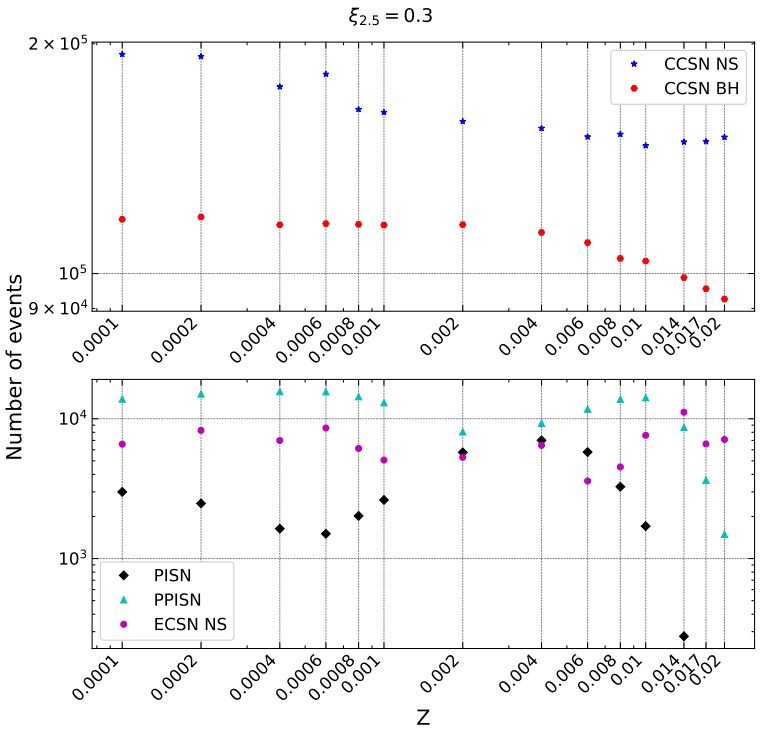

Figure 5.14: Same as Fig. 5.10, but for the *Compactness* model with $\xi_t = 0.3$ (M20).

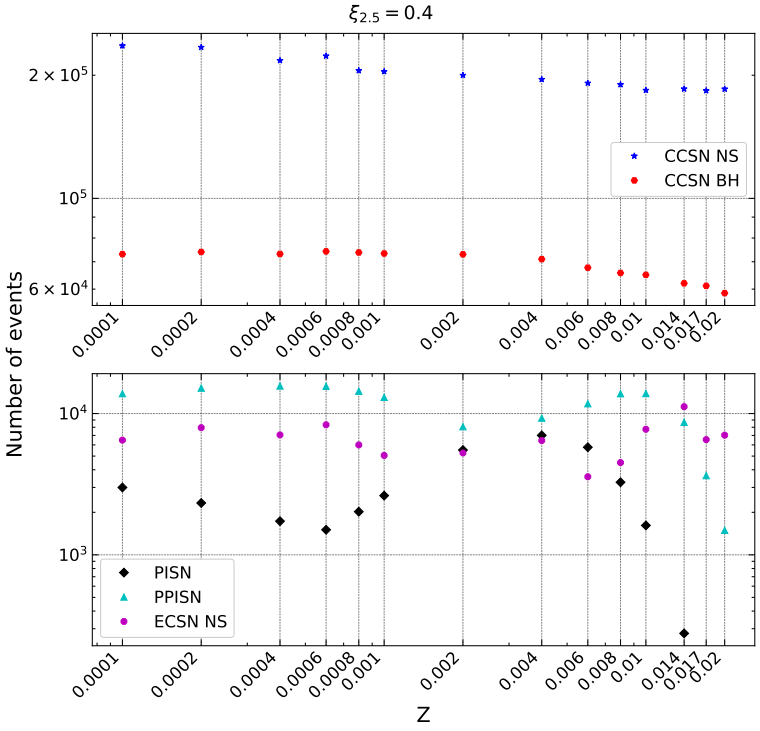

Figure 5.15: Same as Fig. 5.10, but for the *Compactness* model with $\xi_t = 0.4$ (M20).

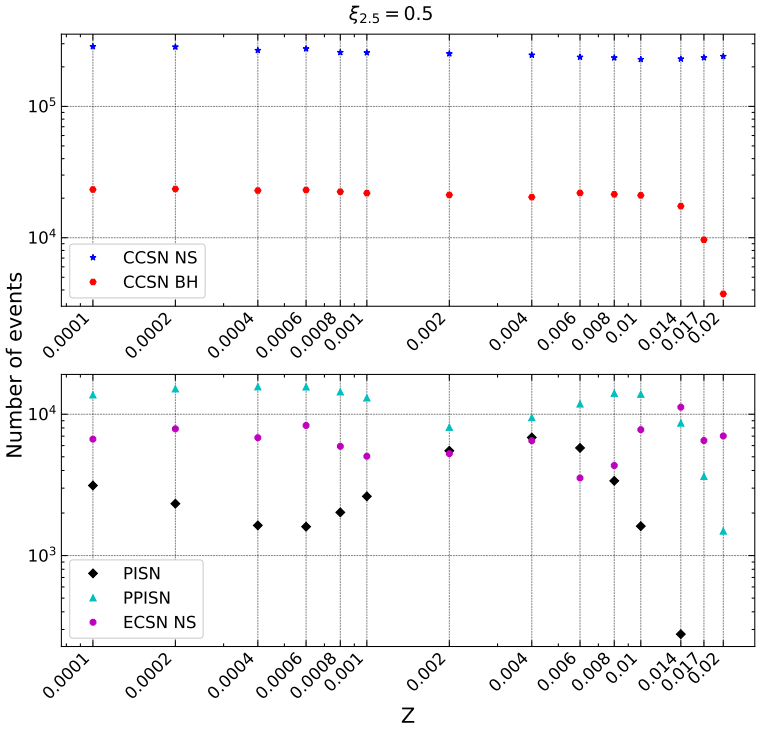

Figure 5.16: Same as Fig. 5.10, but for the *Compactness* model with $\xi_t = 0.5$ (M20).

holes or black holes in loose binary systems, because mass transfer and common envelope tend to remove the H-rich envelopes of the stars, producing smaller black holes.

The lower edge of the black hole mass distribution, instead, shows the effect of mass transfer which lowers the limit for the minimum ZAMS mass. It is exactly in the lower part of the spectrum where we see an overdensity of BHs (figure 5.6), which corresponds indeed to the region mostly populated by BBH mergers (e.g., figure 5.7 bottom panel). This feature is due to the adopted IMF (4.1.4, Kroupa [2001]), which generates a decreasing number of initial stars as the mass increases and allows the formation of most of the black holes in the initial part of the spectrum.

The structure of the mass distributions is similar to the one obtained by LVK collaboration and described in section 2.3 figure 2.3. The models which show a first peak around $10\,M_\odot$ are rapid, delayed, $\xi_t = 0.2$, 0.3, 0.4 (figures 5.7,5.8, 5.9). Multiple peaks are more appreciable in the compactness model, but still they are not well defined. The upper mass limit for BBH mergers is for every model at $\sim 50\,M_\odot$. This is expected, since it is the predicted lower edge of the pair instability region, where the progenitor are completely destroyed leaving no compact remnants.

Mass distributions and supernova counts presented in the previous section were obtained from M20 model. The results for F19 are presented in the appendix [6] for which are valid the same arguments discussed up to now.

Chapter 6

Conclusions

In this thesis, using the population synthesis code SEVN, I have investigated the impact of different CCSN models on the population of BBHs. SEVN calculates stellar evolution by reading a set of pre-computed stellar tracks and includes binary evolution processes by means of analytic and semi-analytic prescriptions. I have simulated the evolution of a set of single stars, starting from an IMF in the range [10, 150] $M_\odot$, and a set of isolated binary systems with ZAMS primary mass between $5\,M_\odot$ and $150\,M_\odot$. The spin of the stars was set to zero and the metallicity was fixed at the beginning of each simulation to values in the range $Z = 2 \times 10^{-2} \div 10^{-4}$. I have used two different PISN models, M20 [Mapelli et al., 2020] and F19 [Farmer et al., 2019], which consider the pre-supernova He-core mass and the pre-supernova CO mass, respectively, to estimate the regions of PPISN and PISN. For each simulation I adopted three different CCSN models: rapid, delayed [Fryer et al., 2012] and compactness [O'Connor and Ott, 2011], using five different compactness thresholds $\xi_t = 0.1, 0.2, 0.3, 0.4, 0.5$.

I have firstly analysed the outputs of the SSE case. In this scenario it was possible to understand the impact of metallicity, CCSN model and PISN model on the BH population (see figures 5.1-5.5). The metallicity determines the production of heavy BHs. For metal-rich stars at $Z = 0.02$ the heaviest BH produced has a mass of $\approx 25\,M_\odot$, while for metal-poor stars (e.g., $Z = 10^{-4}$) the maximum BH mass can reach $90\,M_\odot$ with M20 and $100\,M_\odot$ with F19. CCSN models, instead, mostly affect the lower edges of the BH mass distribution: with the rapid model, the lightest BH is at $5\,M_\odot$ and reproduces the upper edge of the observed mass gap between NSs and BHs ($2 - 5\,M_\odot$); the delayed model instead does not predict any gap, with the transition between NS and BH at $3\,M_\odot$; for the compactness model the lightest BH produced depends on the threshold ξ_t. As the threshold increases, so does the minimum BH mass. The PISN model determines the sharp drops in the mass spectra, because when a star enters the PPISN region it loses mass through a succession of pulses until it reaches the stable region of CCSN. Consequently, the BH formed is less massive. Fluctuations in the spectra are caused by dredge up events, which decrease the mass of the core allowing stars to exit the PPISN regime.

From the binary stellar evolution (BSE) case, it was possible to visualize the effect of binary interactions on the population of BHs (figure 5.6). The primary stars (the heaviest in the binary) tend to donate mass and the resulting BH mass is lower than what it would be if they were single stars. For the opposite reason, secondary stars accrete mass and are able to form heavier BHs with respect to the SSE case.

With these binary simulations it was also possible to study the mass distribution of

BBH mergers with different CCSN models (figures 5.7-5.9). It shows the peculiar peak around $10\,M_\odot$ for all the models (except for $\xi_t = 0.5$) and then a decrease in the number of BHs until the upper mass limit is reached. This corresponds to the lower edge of the pair-instability mass gap. For almost every model the limit is placed between $50\,M_\odot$ and $60\,M_\odot$. Above it, stars undergo PISN and no compact remnant is created.

Finally, I have also quantified the incidence of different supernova types for each CCSN model and for each metallicity (figures 5.10-5.16). I found that the number of ECSNe is $2 - 4\%$ of that of CCSNe, which is in good agreement with observational results of Thompson et al. [2009].

Overall, CCSN models have a crucial impact on the mass function of BBHs. Trying to understand which one better represents the data is fundamental in order to interpret forthcoming gravitational waves signals coming from BBH coalescence.

Bibliography

B. P. Abbott. Observation of gravitational waves from a binary black hole merger. *Phys. Rev. Lett.*, 116:061102, Feb 2016. doi:10.1103/PhysRevLett.116.061102. URL https://link.aps.org/doi/10.1103/PhysRevLett.116.061102.

R. Abbott, T. Abbott, F. Acernese, K. Ackley, C. Adams, N. Adhikari, R. Adhikari, V. Adya, C. Affeldt, D. Agarwal, et al. The population of merging compact binaries inferred using gravitational waves through gwtc-3. *arXiv preprint arXiv:2111.03634*, 2022.

E. G. Adelberger, A. García, R. H. Robertson, K. Snover, A. Balantekin, K. Heeger, M. Ramsey-Musolf, D. Bemmerer, A. Junghans, C. Bertulani, et al. Solar fusion cross sections. ii. the p p chain and cno cycles. *Reviews of Modern Physics*, 83(1):195, 2011.

H. Bondi and F. Hoyle. On the mechanism of accretion by stars. , 104:273, Jan. 1944. doi:10.1093/mnras/104.5.273.

A. Bressan, P. Marigo, L. Girardi, B. Salasnich, C. D. Cero, S. Rubele, and A. Nanni. scpparsec/scp: stellar tracks and isochrones with the PAdova and TRieste stellar evolution code. *Monthly Notices of the Royal Astronomical Society*, 427(1):127–145, oct 2012. doi:10.1111/j.1365-2966.2012.21948.x. URL https://doi.org/10.1111%2Fj.1365-2966.2012.21948.x.

A. Burrows. Neutrinos from supernova explosions. *Annual Review of Nuclear and Particle Science*, 40(1):181–212, 1990.

Y.-Z. Cai, A. Pastorello, M. Fraser, S. Prentice, T. Reynolds, E. Cappellaro, S. Benetti, A. Morales-Garoffolo, A. Reguitti, N. Elias-Rosa, et al. The transitional gap transient at 2018hso: new insights into the luminous red nova phenomenon. *Astronomy & Astrophysics*, 632:L6, 2019.

Y.-Z. Cai, A. Pastorello, M. Fraser, M. Botticella, N. Elias-Rosa, L.-Z. Wang, R. Kotak, S. Benetti, E. Cappellaro, M. Turatto, et al. Intermediate-luminosity red transients: Spectrophotometric properties and connection to electron-capture supernova explosions. *arXiv preprint arXiv:2108.05087*, 2021.

S. Chandrasekhar. The maximum mass of ideal white dwarfs. *The Astrophysical Journal*, 74:81, 1931.

D. D. Clayton. *Principles of stellar evolution and nucleosynthesis*. University of Chicago press, 1983.

J. B. Doggett and D. Branch. A comparative study of supernova light curves. , 90: 2303–2311, Nov. 1985. doi:10.1086/113934.

C. L. Doherty, P. Gil-Pons, L. Siess, and J. C. Lattanzio. Super-AGB stars and their role as electron capture supernova progenitors. *Publications of the Astronomical Society of Australia*, 34, 2017. doi:10.1017/pasa.2017.52. URL https://doi.org/10.1017%2Fpasa.2017.52.

P. P. Eggleton. Aproximations to the radii of Roche lobes. , 268:368–369, May 1983. doi:10.1086/160960.

R. Farmer, M. Renzo, S. de Mink, P. Marchant, and S. Justham. Mind the gap: the location of the lower edge of the pair-instability supernova black hole mass gap. *The Astrophysical Journal*, 887(1):53, 2019.

C. L. Fryer, K. Belczynski, G. Wiktorowicz, M. Dominik, V. Kalogera, and D. E. Holz. COMPACT REMNANT MASS FUNCTION: DEPENDENCE ON THE EXPLOSION MECHANISM AND METALLICITY. *The Astrophysical Journal*, 749(1): 91, mar 2012. doi:10.1088/0004-637x/749/1/91. URL https://doi.org/10.1088%2F0004-637x%2F749%2F1%2F91.

A. Gal-Yam. The Most Luminous Supernovae. , 57:305–333, Aug. 2019. doi:10.1146/annurev-astro-081817-051819.

A. Heger, C. L. Fryer, S. E. Woosley, N. Langer, and D. H. Hartmann. How Massive Single Stars End Their Life. , 591(1):288–300, July 2003. doi:10.1086/375341.

S. Hekker, G. C. Angelou, Y. Elsworth, and S. Basu. Mirror principle and the red-giant bump: the battle of entropy in low-mass stars. *Monthly Notices of the Royal Astronomical Society*, 492(4):5940–5948, jan 2020. doi:10.1093/mnras/staa176. URL https://doi.org/10.1093%2Fmnras%2Fstaa176.

W. Hillebrandt and J. C. Niemeyer. Type ia supernova explosion models. *Annual Review of Astronomy and Astrophysics*, 38(1):191–230, sep 2000. doi:10.1146/annurev.astro.38.1.191. URL https://doi.org/10.1146%2Fannurev.astro.38.1.191.

S. Horiuchi, K. Nakamura, T. Takiwaki, K. Kotake, and M. Tanaka. The red supergiant and supernova rate problems: implications for core-collapse supernova physics. *Monthly Notices of the Royal Astronomical Society: Letters*, 445(1):L99–L103, sep 2014. doi:10.1093/mnrasl/slu146. URL https://doi.org/10.1093%2Fmnrasl%2Fslu146.

J. R. Hurley, C. A. Tout, and O. R. Pols. Evolution of binary stars and the effect of tides on binary populations. *Monthly Notices of the Royal Astronomical Society*, 329 (4):897–928, 2002.

H. T. Janka, K. Langanke, A. Marek, G. Martínez-Pinedo, and B. Müller. Theory of core-collapse supernovae. , 442(1-6):38–74, Apr. 2007. doi:10.1016/j.physrep.2007.02.002.

P. Kroupa. On the variation of the initial mass function. *Monthly Notices of the Royal Astronomical Society*, 322(2):231–246, 2001. doi:10.1046/j.1365-8711.2001.04022.x.

C. Leitherer, C. Robert, and L. Drissen. Deposition of Mass, Momentum, and Energy by Massive Stars into the Interstellar Medium. , 401:596, Dec. 1992. doi:10.1086/172089.

W. Li, J. Leaman, R. Chornock, A. V. Filippenko, D. Poznanski, M. Ganeshalingam, X. Wang, M. Modjaz, S. Jha, R. J. Foley, and N. Smith. Nearby supernova rates from the lick observatory supernova search - II. the observed luminosity functions and fractions of supernovae in a complete sample. *Monthly Notices of the Royal Astronomical Society*, 412(3):1441–1472, mar 2011. doi:10.1111/j.1365-2966.2011.18160.x. URL https://doi.org/10.1111%2Fj.1365-2966.2011.18160.x.

M. Limongi and A. Chieffi. Presupernova evolution and explosive nucleosynthesis of rotating massive stars in the metallicity range- 3[fe/h] 0. *The Astrophysical Journal Supplement Series*, 237(1):13, 2018.

K. Maeda and Y. Terada. Progenitors of type ia supernovae. *International Journal of Modern Physics D*, 25(10):1630024, aug 2016. doi:10.1142/s021827181630024x. URL https://doi.org/10.1142%2Fs021827181630024x.

M. Maggiore. *Gravitational waves: Volume 1: Theory and experiments*. OUP Oxford, 2007.

M. Mapelli. Formation channels of single and binary stellar-mass black holes. *Handbook of gravitational wave astronomy*, pages 705–769, 2022.

M. Mapelli, M. Spera, E. Montanari, M. Limongi, A. Chieffi, N. Giacobbo, A. Bressan, and Y. Bouffanais. Impact of the rotation and compactness of progenitors on the mass of black holes. *The Astrophysical Journal*, 888(2):76, jan 2020. doi:10.3847/1538-4357/ab584d. URL https://doi.org/10.3847%2F1538-4357%2Fab584d.

P. Mazzali, T. Moriya, M. Tanaka, and S. Woosley. The nature of pisn candidates: clues from nebular spectra. *Monthly Notices of the Royal Astronomical Society*, 484(3):3451–3462, 2019.

T. J. Moriya, K. C. Wong, Y. Koyama, M. Tanaka, M. Oguri, S. Hilbert, and K. Nomoto. Searches for population iii pair-instability supernovae: Predictions for ultimate-subaru and wfirst. *Publications of the Astronomical Society of Japan*, 71(3):59, 2019.

E. O'Connor and C. D. Ott. BLACK HOLE FORMATION IN FAILING CORE-COLLAPSE SUPERNOVAE. *The Astrophysical Journal*, 730(2):70, mar 2011. doi:10.1088/0004-637x/730/2/70. URL https://doi.org/10.1088%2F0004-637x%2F730%2F2%2F70.

A. Pastorello and M. Fraser. Supernova impostors and other gap transients. *Nature Astronomy*, 3(8):676–679, aug 2019. doi:10.1038/s41550-019-0809-9. URL https://doi.org/10.1038%2Fs41550-019-0809-9.

A. Pastorello, E. Mason, S. Taubenberger, M. Fraser, G. Cortini, L. Tomasella, M. T. Botticella, N. Elias-Rosa, R. Kotak, S. J. Smartt, S. Benetti, E. Cappellaro, M. Turatto, L. Tartaglia, S. G. Djorgovski, A. J. Drake, M. Berton, F. Briganti, J. Brimacombe, F. Bufano, Y. Z. Cai, S. Chen, E. J. Christensen, F. Ciabattari, E. Congiu, A. Dimai, C. Inserra, E. Kankare, L. Magill, K. Maguire, F. Martinelli, A. Morales-Garoffolo, P. Ochner, G. Pignata, A. Reguitti, J. Sollerman, S. Spiro, G. Terreran, and D. E. Wright. Luminous red novae: Stellar mergers or giant eruptions? , 630:A75, Oct. 2019. doi:10.1051/0004-6361/201935999.

P. C. Peters. Gravitational radiation and the motion of two point masses. *Phys. Rev.*, 136:B1224–B1232, Nov 1964. doi:10.1103/PhysRev.136.B1224. URL https://link.aps.org/doi/10.1103/PhysRev.136.B1224.

P. Podsiadlowski. The evolution of binary systems. *Accretion Processes in Astrophysics*, page 45, 2014.

A. J. T. Poelarends, F. Herwig, N. Langer, and A. Heger. The Supernova Channel of Super-AGB Stars. , 675(1):614–625, Mar. 2008. doi:10.1086/520872.

C. L. Ransome, S. M. Habergham-Mawson, M. J. Darnley, P. A. James, A. V. Filippenko, and E. M. Schlegel. A systematic reclassification of type IIn supernovae. *Monthly Notices of the Royal Astronomical Society*, 506(4):4715–4734, jul 2021. doi:10.1093/mnras/stab1938. URL https://doi.org/10.1093%2Fmnras%2Fstab1938.

H. Sana, S. E. de Mink, A. de Koter, N. Langer, C. J. Evans, M. Gieles, E. Gosset, R. G. Izzard, J.-B. L. Bouquin, and F. R. N. Schneider. Binary interaction dominates the evolution of massive stars. *Science*, 337(6093):444–446, jul 2012. doi:10.1126/science.1223344. URL https://doi.org/10.1126%2Fscience.1223344.

A. Sengupta. The sensitivity of the advanced ligo detectors at the beginning of gravitational wave astronomy. 2016.

S. J. Smartt, J. J. Eldridge, R. M. Crockett, and J. R. Maund. The death of massive stars - i. observational constraints on the progenitors of type II-p supernovae. *Monthly Notices of the Royal Astronomical Society*, 395(3):1409–1437, may 2009. doi:10.1111/j.1365-2966.2009.14506.x. URL https://doi.org/10.1111%2Fj.1365-2966.2009.14506.x.

M. Spera, M. Mapelli, N. Giacobbo, A. A. Trani, A. Bressan, and G. Costa. Merging black hole binaries with the SEVN code. *Monthly Notices of the Royal Astronomical Society*, 485(1):889–907, feb 2019. doi:10.1093/mnras/stz359. URL https://doi.org/10.1093%2Fmnras%2Fstz359.

T. A. Thompson, J. L. Prieto, K. Z. Stanek, M. D. Kistler, J. F. Beacom, and C. S. Kochanek. A New Class of Luminous Transients and a First Census of their Massive Stellar Progenitors. , 705(2):1364–1384, Nov. 2009. doi:10.1088/0004-637X/705/2/1364.

V. Tiwari and S. Fairhurst. The emergence of structure in the binary black hole mass distribution. *The Astrophysical Journal Letters*, 913(2):L19, may 2021. doi:10.3847/2041-8213/abfbe7. URL https://doi.org/10.3847%2F2041-8213%2Fabfbe7.

S. D. Van Dyk, C. Y. Peng, J. Y. King, A. V. Filippenko, R. R. Treffers, W. Li, and M. W. Richmond. SN 1997bs in M66: Another Extragalactic η Carinae Analog? , 112 (778):1532–1541, Dec. 2000. doi:10.1086/317727.

J. S. Vink, A. de Koter, and H. Lamers. Mass-loss predictions for o and b stars as a function of metallicity. *Astronomy & Astrophysics*, 369(2):574–588, 2001.

J. S. Vink, L. E. Muijres, B. Anthonisse, A. de Koter, G. Gräfener, and N. Langer. Wind modelling of very massive stars up to 300 solar masses. , 531:A132, July 2011. doi:10.1051/0004-6361/201116614.

S. Wanajo, K. Nomoto, H. T. Janka, F. S. Kitaura, and B. Müller. Nucleosynthesis in Electron Capture Supernovae of Asymptotic Giant Branch Stars. , 695(1):208–220, Apr. 2009. doi:10.1088/0004-637X/695/1/208.

S. E. Woosley. Pulsational pair-instability supernovae. *The Astrophysical Journal*, 836(2): 244, feb 2017. doi:10.3847/1538-4357/836/2/244. URL https://doi.org/10.3847%2F1538-4357%2F836%2F2%2F244.

S. E. Woosley, A. Heger, and T. A. Weaver. The evolution and explosion of massive stars. *Reviews of modern physics*, 74(4):1015, 2002.

F. Özel and P. Freire. Masses, radii, and the equation of state of neutron stars. *Annual Review of Astronomy and Astrophysics*, 54(1):401–440, sep 2016. doi:10.1146/annurev-astro-081915-023322. URL https://doi.org/10.1146%2Fannurev-astro-081915-023322.

Appendix

Supplementary figures

Mass distribution F19

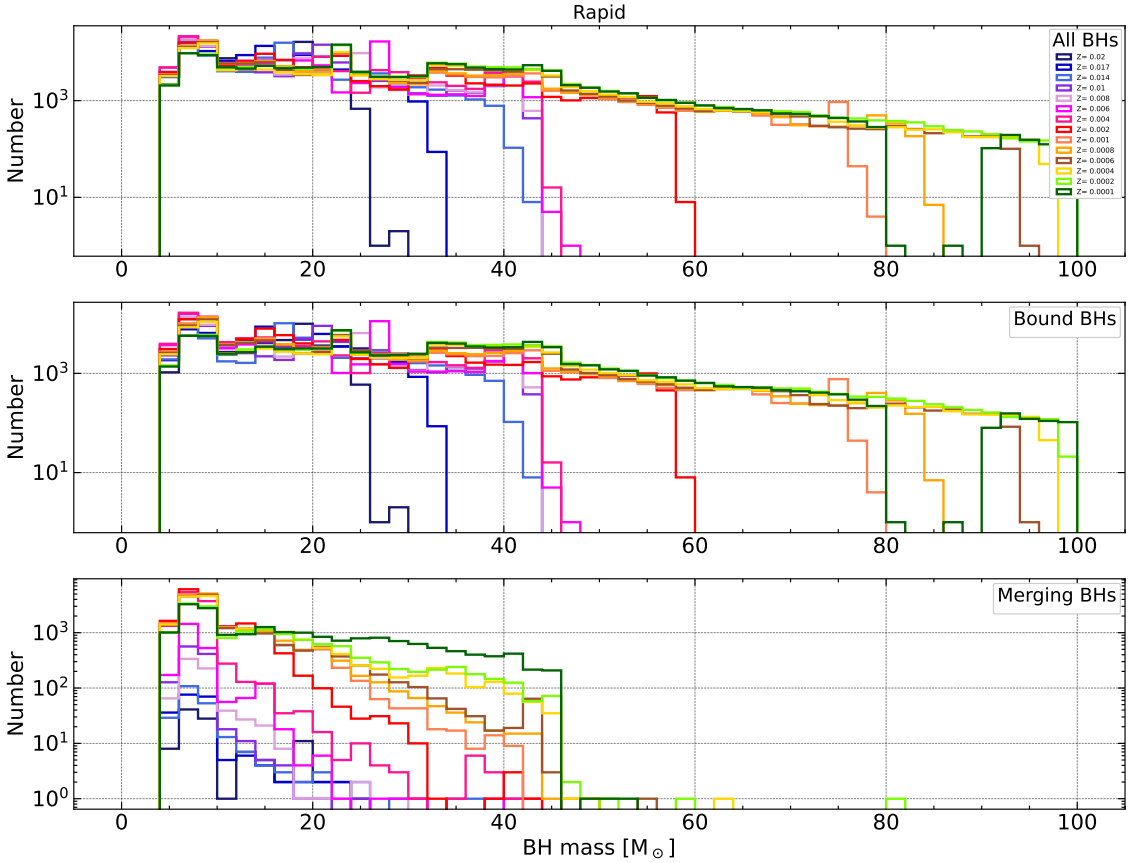

Figure 6.1: Rapid F19

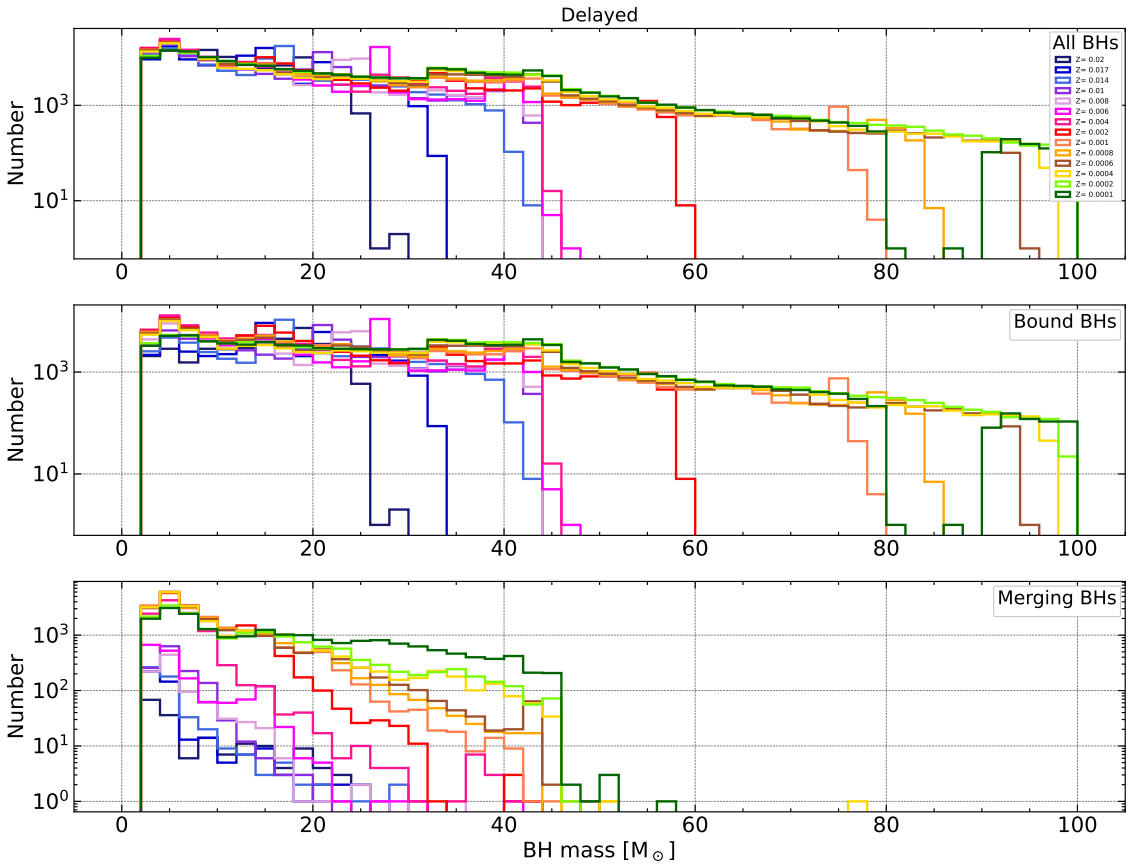

Figure 6.2: Delayed F19

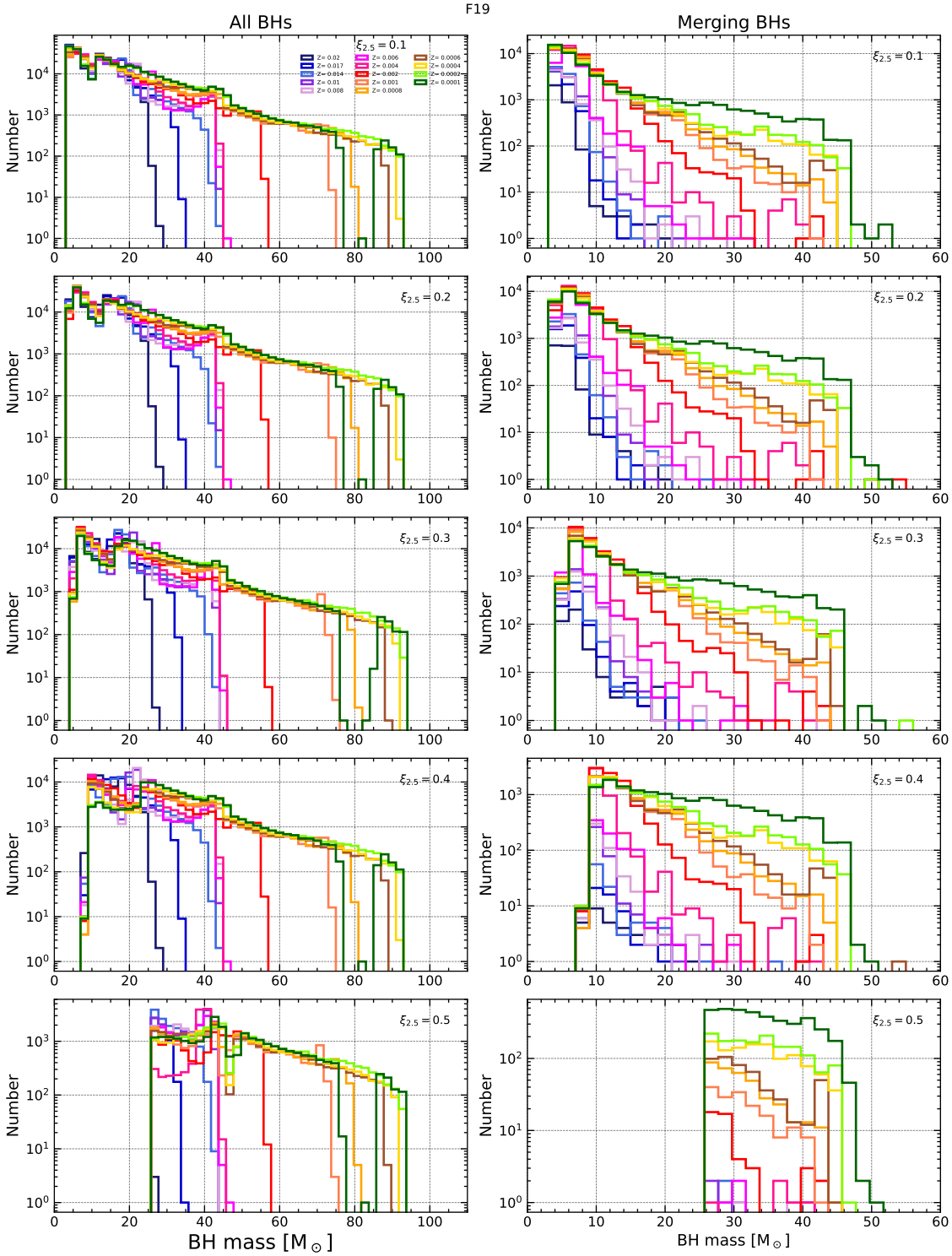

Figure 6.3: Compactness F19

Supernova events F19

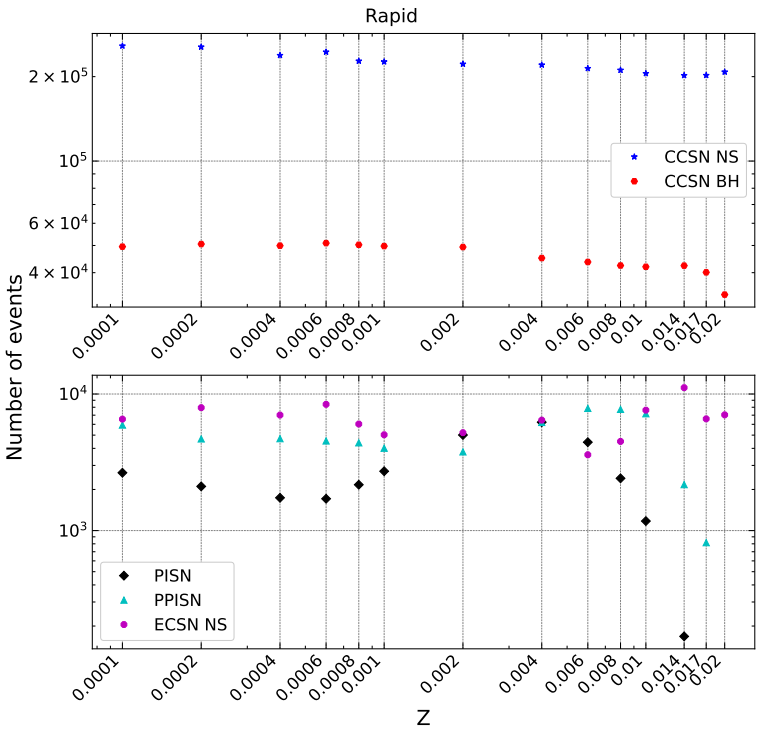

Figure 6.4: Number of supernova events. Rapid F19

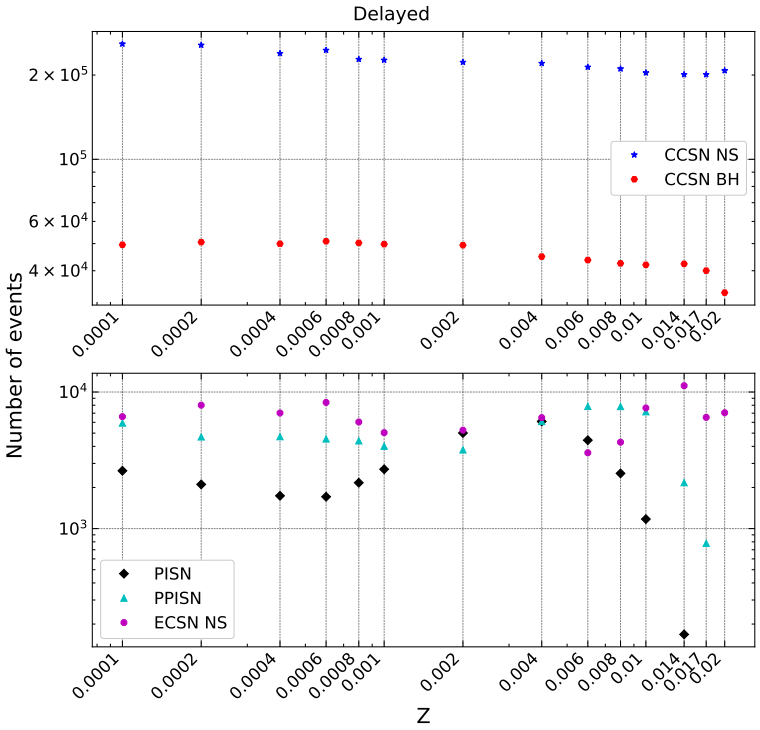

Figure 6.5: Number of supernova events. Delayed F19

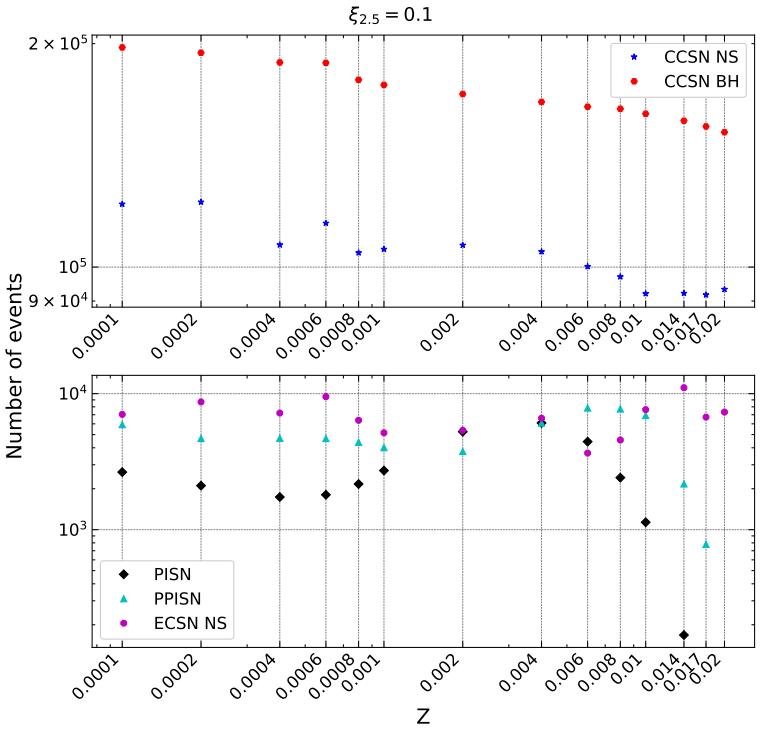

Figure 6.6: Number of supernova events. Compactness $\xi_t = 0.1$ F19

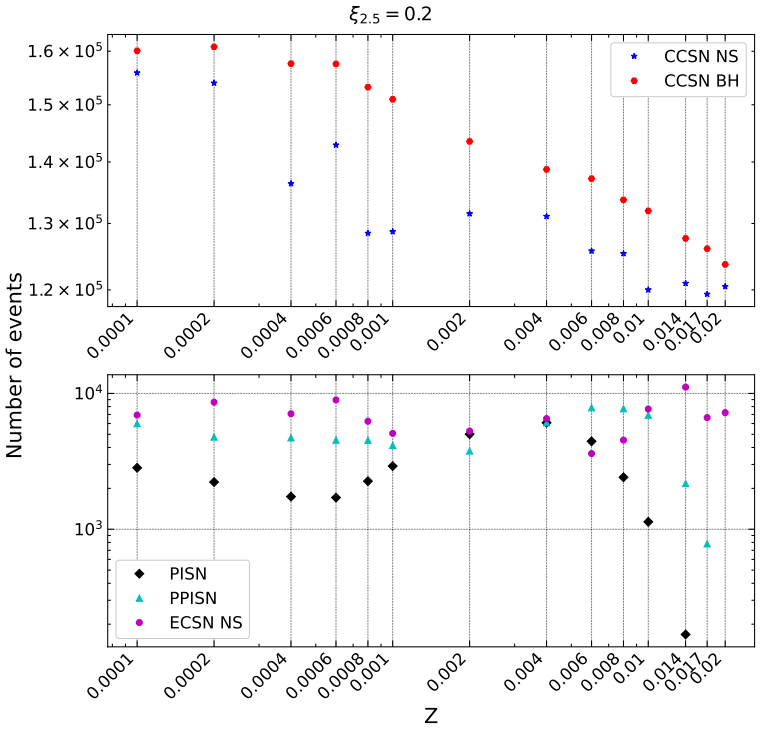

Figure 6.7: Number of supernova events. Compactness $\xi_t = 0.2$ F19

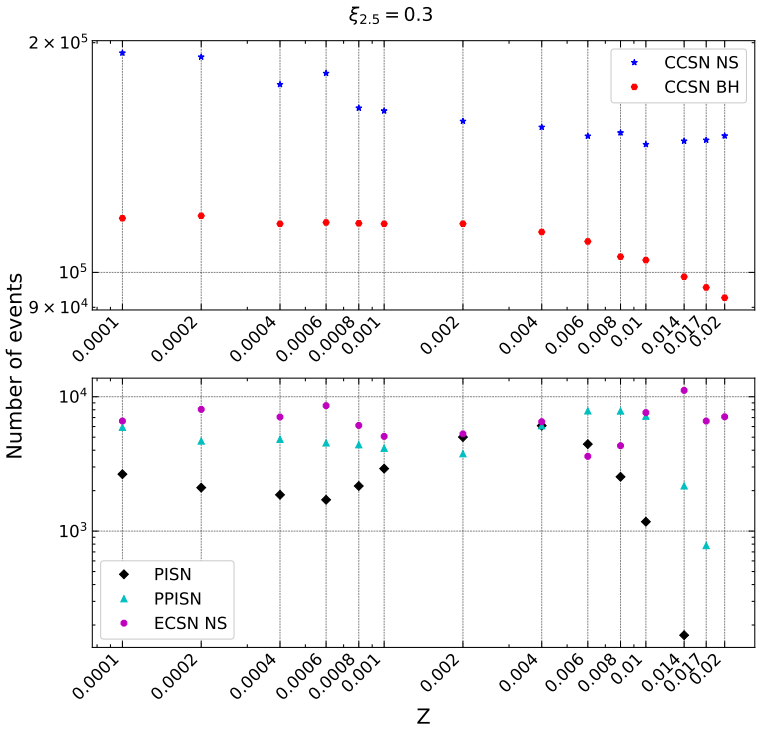

Figure 6.8: Number of supernova events. Compactness $\xi_t = 0.3$ F19

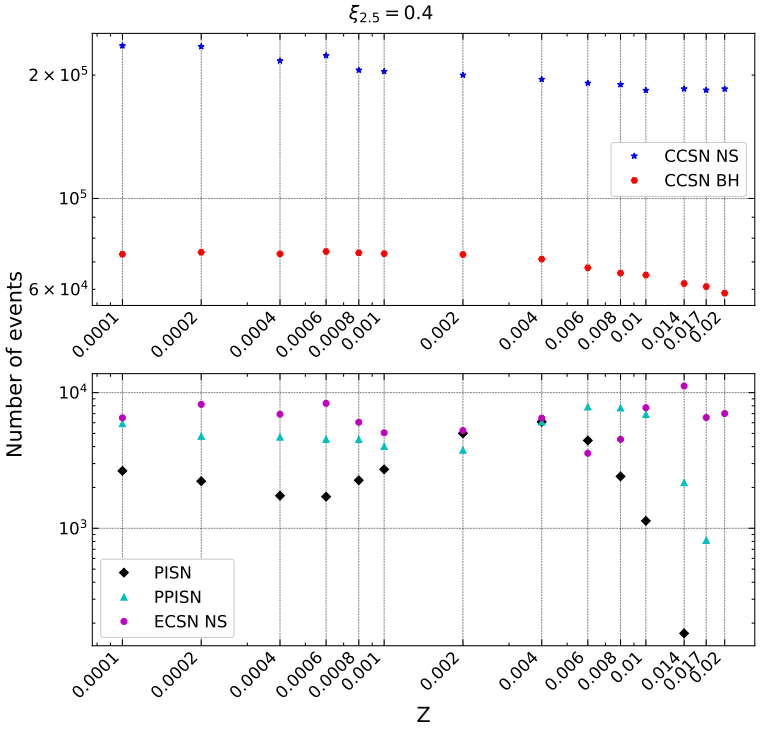

Figure 6.9: Number of supernova events. Compactness $\xi_t = 0.4$ F19

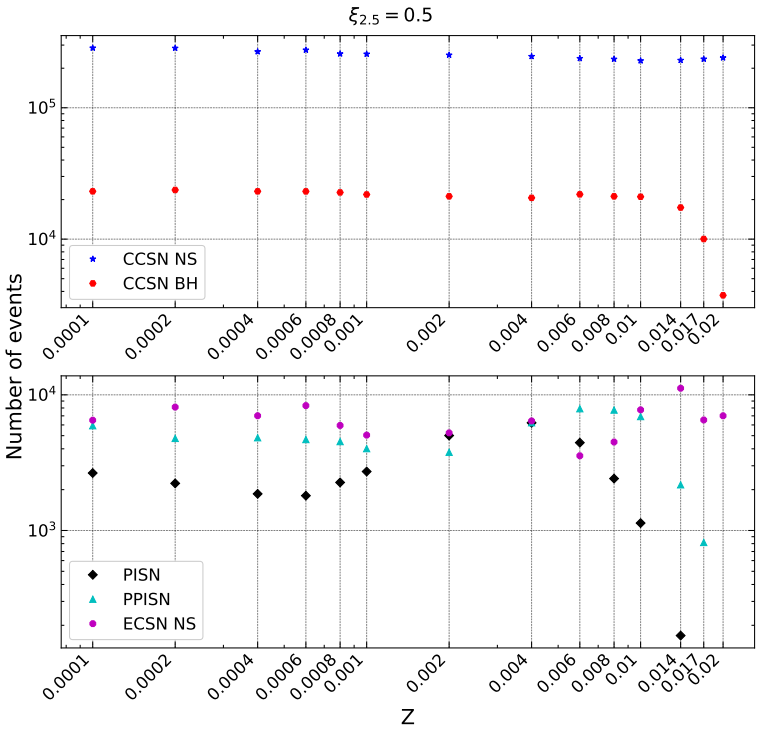

Figure 6.10: Number of supernova events. Compactness $\xi_t = 0.5$ F19